Intelligent computing for electromagnetohydrodynamic bioconvection flow of micropolar nanofluid with thermal radiation and stratification: Levenberg–Marquardt backpropagation algorithm

Cite as: AIP Advances 14, 035224 (2024); doi: 10.1063/5.0187124
Submitted: 15 November 2023 • Accepted: 16 February 2024 •
Published Online: 12 March 2024

Zeeshan Khan,[1] Wafa F. Alfwzan,[2] Aatif Ali,[3,a)] Nisreen Innab,[4,a)] Samina Zuhra,[5] Saeed Islam,[1] and Joshua Kiddy K. Asamoah[6,7,a)]

AFFILIATIONS

[1] Department of Mathematics, Abdul Wali Khan University Mardan, Khyber Pakhtunkhwa 23200, Pakistan
[2] Department of Mathematical Sciences, College of Science, Princess Nourah Bint Abdulrahman University, P.O. Box 84428, Riyadh 11671, Saudi Arabia
[3] School of Mathematical Sciences, Jiangsu University, Zhenjiang, Jiangsu 212013, China
[4] Department of Computer Science and Information Systems, College of Applied Sciences, AlMaarefa University, Diriyah, 13713 Riyadh, Saudi Arabia
[5] Department of Computing and Technology, Abasyn University, Peshawar 25000, Pakistan
[6] Department of Mathematics, Saveetha School of Engineering SIMATS, Chennai, India
[7] Kwame Nkrumah University of Science and Technology, Kumasi, Ghana

[a)] **Authors to whom correspondence should be addressed:** atifkh98@gmail.com; ninnab@um.edu.sa; and jkkasamoah@knust.edu.gh

ABSTRACT

The Levenberg–Marquardt (LM) backpropagation optimization algorithm, an artificial neural network algorithm, is used in this study to perform integrated numerical computing to evaluate the electromagnetohydrodynamic bioconvection flow of micropolar nanofluid with thermal radiation and stratification. The model is then reduced to a collection of boundary value problems, which are solved with the help of a numerical technique and the proposed scheme, i.e., the LM algorithm, which is an iterative approach to determine the minimum of a nonlinear function defined as the sum of squares. As a blend of the steepest descent and the Gauss–Newton method, it has become a typical approach for nonlinear least-squares problems. Furthermore, the stability and consistency of the algorithm are ensured. For validation purposes, the results are also compared with those of previous research and the MATLAB bvp4c solver. Neural networking is also utilized for velocity, temperature, and concentration profile mapping from input to output. These findings demonstrate the accuracy of forecasts and optimizations produced by artificial neural networks. The performance of the bvp4c solver, which is used to reduce the mean square error, is used to generalize a dataset. The artificial neural network-based LM backpropagation optimization algorithm operates using data based on the ratio of testing (13%), validation (17%), and training (70%). This stochastic computing work presents an activation log-sigmoid function based LM backpropagation optimization algorithm, in which tens of neurons and hidden and output layers are used for solving the learning language model. The overlapping of the results and the small computed absolute errors, which range from 10^{-3} to 10^{-10} and from 10^{6} to 10^{8} for each model class, indicate the accuracy of the artificial neural network-based LM backpropagation optimization algorithm. Furthermore, each model case's regression performance is evaluated as if it were an ideal model. In addition, function fitness and histogram are used to validate the dependability of the algorithm. Numerical approaches and artificial neural networks are an excellent combination for fluid dynamics, and this could lead to new advancements in many domains. The findings of this research could contribute to the optimization of fluid systems, resulting in increased efficiency and production across various technical domains.

 https://doi.org/10.1063/5.0187124

NOMENCLATURE

a	Constant term in the stretching sheet
b_1, b_2, d_1, d_2, e_1, and e_2	Constants of coefficient
$\hat{C}, \hat{C}_\infty, \hat{C}_w$	Fluid, ambient, and surface fluid concentration, respectively
$\hat{D}_{\hat{n}}, \hat{D}_{\hat{T}}, \hat{D}_B$	Diffusivities of microorganism concentration, nanofluidic temperature, and nanofluid concentration, respectively
$\hat{E} = \left(0, 0, -\hat{E}_0\right), B = \left(0, \hat{B}_0, 0\right)$	Electric and magnetic forces, respectively
$g, \hat{N}, \hat{\sigma}, \beta$	Gravitational force, angular velocity, electrical conductivity, and volume expansion coefficient, respectively
K, S, Nr, and Q	Micropolar constant, thermal stratification, buoyancy ratio, and mass stratification parameters, respectively
K_f^*, $j = \frac{\nu_f}{a}$	Vertex viscosity and micro-inertia density, respectively
M, Nt, E, and Rd	Magnetic, thermophoretic, and activation energy and thermal radiation parameters, respectively
$\hat{n}, \hat{n}_\infty, \hat{n}_w$	Concentration of the microorganism and ambient/surroundings and surface concentration of microorganisms, respectively
Pr, Pe, Lb, and Ec	Prandtl, Peclet, Lewis bioconvection, and Eckert numbers, respectively
$\hat{\rho}_p, \hat{\rho}_m, \hat{\rho}_f$	Density of the nanoparticle, microorganism, and fluid, respectively
Q_0, $\frac{bW_c}{\Delta C} * \nabla C$, W_c	Heat generation rate, average velocity, and speed of the microorganism during swimming, respectively
$Rb, Gr, \mathrm{Re}_{\hat{x}}, Sc$	Bioconvection Rayleigh, local Grashof, Reynolds, and Schmidt numbers, respectively
$\hat{T}, \hat{T}_\infty, \hat{T}_w$	Fluid, ambient, and surface fluid temperature, respectively
$\tau = \frac{(\hat{\rho c})_p}{(\hat{\rho c})_f}, \alpha = \frac{k_f}{(\hat{\rho c})_f}$	Effectiveness heat capacity of nanoparticles to heat capacity of fluid and thermal diffusivity number, respectively
$\hat{x}, \hat{y}$	Cartesian coordinates
δ, Nb, B, and Ω	Heat generation coefficient, Brownian motion, motile density stratification, and microorganism concentration difference parameters, respectively
$\lambda, Gc_x, E1$, and λ_1	Mixed convection, modified number for the local Grashof, and electric and heat generation or absorption parameters, respectively

Abbreviations

AI	Artificial intelligence
ANN-LMBOA	Artificial neural networks Levenberg–Marquardt (LM) backpropagation optimization algorithm
BCMN	Bioconvection flow of micropolar nanofluid
CBL	Concentration boundary-layer
EHs	Error histograms
EMHD	Electromagnetohydrodynamic
MBL	Momentum boundary-layer
MSE	Mean squared error
NNs	Neural networks
ODEs	Ordinary differential equations
PDEs	Partial differential equations
R	Coefficient of determination
TBL	Thermal boundary-layer
TRS	Thermal radiation and stratification

I. INTRODUCTION

It is imperative that the thermal properties of nanofluids in thermal engineering, including thermal conductivity, diffusivity, viscosity, and thermal transit, be enhanced. There are a variety of components at the nanoscale suspended in the host fluid. However, the term "nanofluid" is often used to refer to the colloidal suspension of one or more of these components.[1] With a liquid phase for the base fluid and bulk nanomaterial, it is a two-phase system. Almost every industrial and technical field, from the car sector to the medical field, may benefit from the usage of nanofluid. By heating hydraulic fluid, nuclear reactors and geothermal installations might all benefit from its utilization. In vehicle components, nanofluid is used as transmission fluid such as coolants, lubricating oils, and other consumables. Nano-drug delivery, cryopreservation, cancer therapy, nano-cryosurgery, sensing, and imaging are all examples of how this technology is used in biomedicine. Microchips, for example, are cooled by nanofluid in industrial equipment.[2] Despite its great value, the two-phase structure of this field presents a number of difficulties. Stability analysis has been the subject of several experiments and theoretical research in an attempt to improve the thermophysical properties at a low laboratory cost. Keeping nanoparticles in the base fluid over the long term is still a challenge. Because of this, scientists are working hard to develop nanofluids via theoretical[3,4] or experimental research[5,6] in order to increase their thermal performance and solve their long-term stability issue. Nanofluids possess enough stability and enough viscoelasticity and have superior saturating, distributing, and diffusion capabilities on solid surfaces, which are some of their main benefits.[7] In addition, the fluidic movement in the context of a magnetic ground has crucial uses in metallurgical,

chemical, manufacturing, and other scientific fields. Regulating the pace of cooling requires magnetic field-exposed electrically conducting fluid. Regulating the rate of cooling may improve the final product. Magnetic particles play a key role in the production of loud speakers, in the treatment of cancer, and in the separation of sink floats. There are a few helpful recent studies on nanofluids, such as Refs. 8–13.

Fluids that are non-Newtonian (rheological) are used in a variety of manufacturing processes. These fluids have properties that differ greatly from those of viscous Newtonian fluidic models. Numerous models of non-Newtonian fluids exist, notably shear thinning pseudo-plastics and visco-plastics (Bingham, Maxwell, and Oldroyd-B). However, such types of models just alter the shear stress tensor and do not take the impact of the microstructure into account. Fluids used in many materials processing procedures contain a microstructure, that is, the particles floating in the liquids may spin. Using normal non-Newtonian models, it is impossible to reproduce such phenomena. In response to this, Eringen[14] created a new area of fluid dynamics in the 1960s called "micro-morphic fluid mechanics" that accurately models the angular velocity. The concept of micro-rotation of particles in non-Newtonian fluids is introduced.[15] The micropolar model[16] is a new version of the generic "micro-morphic fluid model" that reduces the degrees of freedom of the particles and ignores the axial compression of micro-elements. As a result, micropolar theory has been widely used in a variety of high-quality investigations because it correctly simulates colloidal dispersions, smart fluids, and biologically fluent media (such as blood and articular fluid) in a variety of ways. Another benefit of the micropolar fluid theory is that the Navier–Stokes–Newtonian model may be recovered by ignoring the rotation (gyratory motion of micro-elements).[17] Inspired by coatings and adhesives, a large number of academics have examined the micropolar fluids' outer boundary layer flows from various geometries.[18–21]

Micro-organisms are single cells; they survive in animals, humans, and bodies of plants. As micro-organisms are collected, they become the source of bioconvection since they are considerably heavier than water. Gyrotactic bacteria, which are up-swimming micro-organisms due to gravitational instability, exhibit the bioconvection phenomena.[22] The cell-swimming direction in relation to the microbe species is driven by the bioconvection model. The phenomena of bioconvection find several uses in various biological systems, chemical processes, and ecological structures.[23] The use of nanofluid interaction with motile microbes may improve the stability of the suspension. Numerous researchers have noticed this intriguing behavior.[24–31] The integrating effect of micropolar nanofluid on bioconvection phenomena has been described in significant ways by many researchers. Shahzad *et al.*[32] used the bioconvection phenomena in micropolar nanofluid Darcy–Forchheimer flow that pass into double disks and investigated the Brownian motion and thermophoresis diffusivity. Bioconvection containing gyrotactic microbes in micropolar MHD Maxwell nanofluid flow has been studied by Habib *et al.*[33] in an extending sheet. Numerical simulation is carried out by Ali *et al.*[34] for the multi-slip consequence of time dependent magnetohydrodynamic micropolar nanofluid in gyrotactic micro-organism flow past a solutal sheet that has thermal convective boundary conditions. Tlili *et al.*[35] studied the magnetohydrodynamic micropolar nanofluid flow under the effect of double stratification and partial slip.

Computational science has evolved from experimental tactics to model-based theoretical paradigms and finally to the computational paradigm. Information gleaned from numerous techniques is now more sophisticated than we could have imagined. At present, new techniques arise as a fourth paradigm through data-driven established precise forecasts on large datasets and discovery-based data mining tools that overcome the conventional constraints of their predecessors.[36] These three classic modes of scientific research are now backed by the fourth paradigm and the development of new computing technologies such as high-performance computing, machine learning (ML), and data mining.[37]

Artificial neural networks have an explosion of relevant studies that have attempted to connect novel algorithms with human perception.[38] A subset of artificial intelligence (AI) known as machine learning (ML) uses statistical methods to assess and develop algorithms based on data and make predictions about it. These algorithms are categorized into three parts according to dataset. For predictions from labeled data, supervised learning is used, whereas unsupervised learning is used if someone get unlabeled data. During supervised learning, data from the training set are used to determine how inputs and outputs are related. In unsupervised learning, the initial step is to look for patterns in the incoming data. There have been a significant number of new evaluations and viewpoints on ML and fluids in the last several months. Brunton *et al.*,[39] Sofos *et al.*,[40] Agwu *et al.*,[41] and Zhang and Noack[42] provide a historical assessment of fluid mechanics, identifying previous and present advancements, as well as anticipating the future. In the field of nanofluid, artificial intelligence has shown significant performance in predicting the simulation accuracy of the physical model.[43–45]

In this article, the numerical simulation of magnetohydrodynamic nanofluid flow in a permeable medium is carried out through an unsupervised neural network referred to as the Levenberg–Marquardt backpropagation algorithm. This algorithm is successfully used for the high order nonlinear differential equations.[46–48]

This work presents new insights into the electromagnetohydrodynamic bioconvection flow of micropolar nanofluid flow with thermal radiation and stratification (EMHD-BCMN-TRS) by using sophisticated computational techniques to examine and simulate the complex fluid dynamic behavior of these materials.

In a micropolar nanofluid, thermal radiation, stratification, and the bioconvection flow effect combine to provide a complex problem that is difficult to solve with customary numerical or analytical techniques. Intelligent computer approaches such as fuzzy logic, ANNs, and genetic algorithms provide a useful means of modeling and forecasting the behavior of these materials in intricate fluid systems.

These methods make use of the capabilities of optimization algorithms and machine learning to produce more precise projections and efficiency than those generated with traditional methods. They might also provide insight into the basic physics of the system.

Furthermore, this field of study still has a lot of room for growth and inquiry because intelligent computing is still a relatively new application. These methods have the potential to make difficult problems in micropolar nanofluids, nanofluids, and other fields of fluid mechanics easier to understand and solve. They may also make it easier to develop microfluidic devices that are more effective and efficient. The following are the primary goals of this study:

i. Depict the EMHD-BCMN-TRS mathematical modeling.
ii. Using training, validation, and testing procedures, describe the solution for the intended EMHD-BCMN-TRS fluid model.
iii. Examine the randomly selected reference data samples for testing, training, and validation. Then, compare the estimated solutions of the suggested ANN-LMBOA with the reference outcomes.
iv. Create datasets using LM in the training, validation, and testing phases in order to determine the approximate solution for the suggested ANN-LMBOA algorithm.
v. The proposed method effectively investigates the problem dynamics for various scenarios by varying relevant parameters to illustrate the temperature, concentration, and velocity profiles.
vi. Based on a careful review of the evaluation of accuracy, histograms, and regression analysis performed for the EMHD-BCMN-TRS fluidic model, all of which are provided in sufficient pictorial and numerical detail, the ANN-LMBOA validity and verification are established.
vii. The EMHD-BCMN-TRS fluid model based on ODEs is solved using a log-sigmoid activation function.
viii. Statistical operators based on single/multiple executions have validated the consistency, exactness, and dependability of the stochastic approach in solving the EMHD-BCMN-TRS fluid model.
ix. The different EMHD-BCMN-TRS scenarios are investigated by adjusting the magnetic number, electric parameter, vertex viscosity, chemical reaction, and thermal radiation parameters, as well as mass stratification and Schmidt and Peclet numbers.

II. FLOW CONFIGURATION AND MATHEMATICAL FORMULATION

The primary goal is to explore the unsteady and incompressible two dimensional mixed convection electrically conducting micropolar nanofluid having a magneto-hydrodynamic effect (MHD) that is being passed over a stretchable plate. For the purpose of stabilizing the nanoparticles in the host fluid, bioconvection containing gyrotactic micro-organisms is combined with nanofluids in a way that prevents microbes from changing their swimming direction or their momentum speed as a result of the addition of the nanofluid. Ohm's law, temperature stratification, and thermal radiation are all considered to have an impact on the flow. Cartesian coordinates are assumed in the flow configuration so that the velocity $(\hat{u}(\hat{x}) = a\hat{x})$ is in the horizontal direction of the stretchable sheet whereas the $(\hat{y})$ coordinate is in the vertical direction of the normal stretchable sheet. Beyond the region $(\hat{y} > 0)$, the bioconvection nanofluid flow is thought to be restricted. In the vicinity of positive $(\hat{y})$, constant electric and magnetic forces of strengths $\widehat{E} = \left(0, 0, -\widehat{E}_0\right)$ and $B = \left(0, \widehat{B}_0, 0\right)$ are applied, respectively. In contrast, it is thought that the local Reynolds number is so small that it is practically negligible. The coordinate system for the flow structure is shown in Fig. 1.

Under the aforementioned supposition, the Navier–Stokes equations for the conservation of mass, momentum, angular velocity, energy, nanofluid concentration, and gyrotactic microbial concentration are as follows:[49]

$$\frac{\partial \hat{u}}{\partial \hat{x}} + \frac{\partial \hat{v}}{\partial \hat{y}} = 0, \tag{1}$$

$$\begin{aligned}\hat{u}\frac{\partial \hat{u}}{\partial \hat{x}} + \hat{v}\frac{\partial \hat{u}}{\partial \hat{y}} + = &\left(\widehat{\nu}_f + \frac{\widehat{k}_f}{\widehat{\rho}_f}\right)\frac{\partial^2 \hat{u}}{\partial \hat{y}^2} + \left(\frac{\widehat{k}_f}{\widehat{\rho}_f}\right)\frac{\partial \hat{N}}{\partial \hat{y}} + \frac{\widehat{\sigma}}{\widehat{\rho}_f}E_0\widehat{B}_0 \\ &- \frac{\widehat{\sigma}}{\widehat{\rho}_f}\widehat{B}_0^2\hat{u} + \frac{1}{\widehat{\rho}_f}\left(\left(1-\hat{C}_f\right)\widehat{\rho}_f\beta g\left(\hat{T}-\hat{T}_\infty\right)\right. \\ &- g\left(\widehat{\rho}_p - \widehat{\rho}_f\right)\left(\hat{C}-\hat{C}_f\right) - \gamma^* g(\hat{n}-\hat{n}_\infty) \\ &\left.\times\left(\widehat{\rho}_m - \widehat{\rho}_f\right)\right),\end{aligned} \tag{2}$$

$$\hat{u}\frac{\partial \hat{N}}{\partial \hat{x}} + \hat{v}\frac{\partial \hat{N}}{\partial \hat{y}} + \left(\frac{k_f^*}{\tilde{\rho}_f j_f^*}\right)\left(2\hat{N} + \frac{\partial \hat{u}}{\partial \hat{y}}\right) = \left(\frac{\gamma_f{}^*}{\tilde{\rho} j^*}\right)\frac{\partial^2 \hat{N}}{\partial \hat{y}^2}, \tag{3}$$

$$\begin{aligned}\hat{u}\frac{\partial \hat{T}}{\partial \hat{x}} + \hat{v}\frac{\partial \hat{T}}{\partial \hat{y}} = &\alpha\frac{\partial^2 \hat{T}}{\partial \hat{y}^2} + \tau\left(\frac{\tilde{D}_{\hat{T}}}{\hat{T}_\infty}\left(\frac{\partial \hat{T}}{\partial \hat{y}}\right)^2 + \tilde{D}_B\left(\frac{\partial \hat{C}}{\partial \hat{y}}\frac{\partial \hat{T}}{\partial \hat{y}}\right)\right) \\ &- \frac{1}{\left(\tilde{\rho}\tilde{c}_p\right)_f}\frac{\partial q_r}{\partial \hat{y}} + \frac{\sigma}{\left(\tilde{\rho}\tilde{c}_p\right)_f}\left(\widehat{B}_0\hat{u} - E_0\right)^2 \\ &+ \frac{Q_0}{\left(\tilde{\rho}\tilde{c}_p\right)_f}\left(\hat{T}-\hat{T}_\infty\right),\end{aligned} \tag{4}$$

$$\hat{u}\frac{\partial \hat{C}}{\partial \hat{x}} + \hat{v}\frac{\partial \hat{C}}{\partial \hat{y}} + R^*\left(\hat{C}-\hat{C}_\infty\right) = \frac{\tilde{D}_{\hat{T}}}{\hat{T}_\infty}\frac{\partial^2 \hat{T}}{\partial \hat{y}^2} + \tilde{D}_B\frac{\partial^2 \hat{C}}{\partial \hat{y}^2}, \tag{5}$$

$$\hat{u}\frac{\partial \hat{n}}{\partial \hat{x}} + \hat{v}\frac{\partial \hat{n}}{\partial \hat{y}} + \left\{\frac{\partial}{\partial \hat{y}}\left(\frac{\partial \hat{C}}{\partial \hat{y}}\hat{n}\right)\right\}\frac{bW_c}{\hat{C}_\infty} = \tilde{D}_n\frac{\partial^2 \hat{n}}{\partial \hat{y}^2}. \tag{6}$$

The boundary constraints are[50]

$$\begin{cases}\hat{u} = \hat{u}_w(x) = a\hat{x}, \\ \hat{v} = 0, \\ \hat{N} = 0, \\ \hat{T} = \hat{T}_w = T_0 + b_1\hat{x}, \\ \hat{C} = \hat{C}_w = C_0 + d_1\hat{x}, \\ \hat{n} = \hat{n}_w = n_0 + e_1\hat{x},\end{cases} \quad at \quad \hat{y} = 0, \qquad \begin{cases}\hat{u} \to 0, \\ \hat{N} \to 0, \\ \hat{T} \to \hat{T}_\infty = T_0 + b_2\hat{x}, \\ \hat{C} \to \hat{C}_\infty = C_0 + d_2\hat{x}, \\ \hat{n} \to \hat{n}_\infty = n_0 + e_2\hat{x},\end{cases} \quad at \quad \hat{y} \to \infty. \tag{7}$$

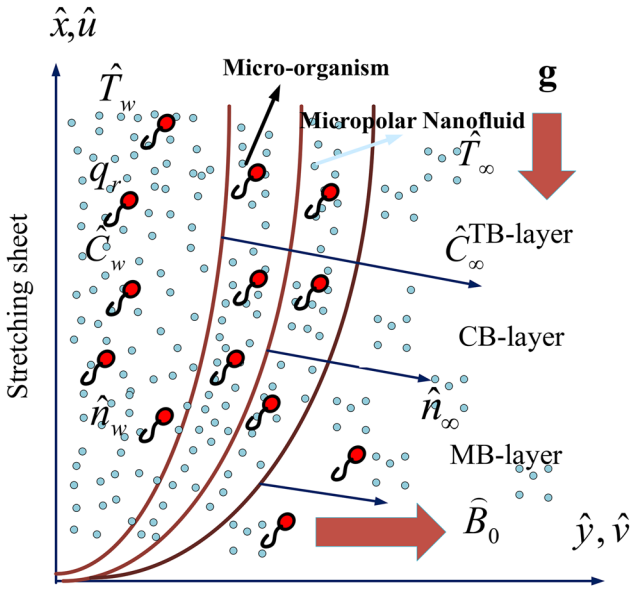

FIG. 1. Geometrical configuration of the model.

The term spin gradient viscosity $\left(\gamma_f^*\right)$ in angular velocity (3) is defined as

$$\gamma_f^* = j\left(\mu_f^* + \frac{1}{2}K_f^*\right). \tag{8}$$

The thermal radiation parameter in Eq. (4) can be written as

$$q_r = 4/3\frac{\sigma^*}{k^*}\frac{\partial \hat{T}_4}{\partial \hat{y}}. \tag{9}$$

Here, $k^* \rightarrow$ average absorption coefficient and $\sigma^* \rightarrow$ constant (Stefan–Boltzmann). The $\hat{T}_4$ Taylor expansion about $\hat{T}_\infty$ is given as

$$\hat{T}_4 \tilde{=} \hat{T}_\infty^4 + 2\left(\hat{T} - \hat{T}_\infty\right)\left(2\hat{T}_\infty^3 + 3\hat{T} - 3\hat{T}_\infty\right) + \cdots. \tag{10}$$

Conversion of governing equations to a system of differential form:

The stream function can be written as $\psi = \psi(x, y)$,

$$\hat{u} = \frac{\partial \psi}{\partial \hat{y}}, \quad \hat{v} = -\frac{\partial \psi}{\partial \hat{x}}. \tag{11}$$

To solve the problem, the set of PDEs has been transformed into a set of ODEs by introducing the stream function equations and similarity transformations. The similarity transformations are chosen as

$$\left.\begin{aligned} \eta &= \hat{y}\sqrt{\frac{a}{\nu}}, & \hat{u} &= a\hat{x}f'(\eta), & \hat{v} &= -(a\nu)^{1/2}f(\eta), \\ \hat{N} &= a\hat{x}\left(\sqrt{\frac{a}{\nu}}\right)g(\eta), & \theta(\eta) &= \frac{\left(\hat{T} - \hat{T}_\infty\right)}{\left(\hat{T}_w - \hat{T}_0\right)}, \\ \phi(\eta) &= \frac{\left(\hat{C} - \hat{C}_\infty\right)}{\left(\hat{C}_w - \hat{C}_0\right)}, & \xi(\eta) &= \frac{\left(\hat{n} - \hat{n}_\infty\right)}{\left(\hat{n}_w - \hat{n}_0\right)}. \end{aligned}\right\} \tag{12}$$

Equation (1) is identically satisfied and Eqs. (2)–(6) take the following form:

$$(1+K)f''' - f'^2 - Mf' + M\hat{E} + ff'' + Kg' + \lambda(\theta + Nr\phi - Rb\Psi) = 0, \tag{13}$$

$$\left(1 + \frac{K}{2}\right)g'' - K(2g + f'') - gf' + g'f = 0, \tag{14}$$

$$\left(1 + \frac{4}{3}Rd\right)\theta'' + \Pr f\theta' + \Pr\left(Nb\theta'\phi' + Nt\theta'^2\right) - \Pr\left(f'\theta + Sf'\right) + \Pr\delta\theta + M^2 Ec\left(f'^2 + \hat{E}^2 - 2\hat{E}f'\right) = 0, \tag{15}$$

$$\phi'' + (Nt/Nb)\theta'' + Sc\left(f\phi' - f'\phi - Qf'\right) = 0, \tag{16}$$

$$\Psi'' - Lb\left(\Psi f' + Bf' - \Psi' f\right) - Pe(\Psi + \Omega)\phi'' - Pe\Psi'\phi' = 0, \tag{17}$$

$$Sc = \frac{\nu_f}{D_B}, \quad Pe = \frac{bW_c}{D_n}, \quad \lambda = \frac{Gr}{\mathrm{Re}_{\hat{x}}^2}, \quad \Pr = \frac{\nu_f}{\alpha'}, \quad M = \frac{\tilde{\sigma}\tilde{B}_0^2}{\alpha\tilde{\rho}_f}, \quad Lb = \frac{\nu_f}{\tilde{D}_n},$$
$$Nt = \frac{\left(\widehat{\rho c_p}\right)_p}{\left(\widehat{\rho c_p}\right)_f}\frac{\tau\tilde{D}_T\left(\hat{T}_w - \hat{T}_\infty\right)}{\nu_f\hat{T}_\infty}, \quad Gr = \frac{\hat{g}\beta_{\hat{C}}\left(1 - \hat{C}_\infty\right)\Delta\hat{x}^3}{\nu_f^2}, \quad Nb = \frac{\left(\widehat{\rho c_p}\right)_p}{\left(\widehat{\rho c_p}\right)_f}\frac{\tilde{D}_B\left(\hat{C}_w - \hat{C}_\infty\right)}{\nu_f},$$
$$Gc_{\hat{x}} = \frac{g\beta_c\left(\hat{C}_w - \hat{C}_\infty\right)}{\hat{x}\alpha^2}, \quad Ec = \frac{a^2\hat{x}^2}{\left(\widehat{\rho c_p}\right)_f\left(\hat{T}_w - \hat{T}_\infty\right)}, \quad K = \frac{k_f^*}{\mu_f}, \tag{18}$$
$$S = \frac{b_2}{b_1}, \quad Q = \frac{d_2}{d_1}, \quad Nr = \frac{\left(\tilde{\rho}_p - \tilde{\rho}_f\right)\left(\hat{C}_w - \hat{C}_0\right)}{\beta\tilde{\rho}_f\left(\hat{T}_w - \hat{T}_0\right)}, \quad \mathrm{Re}_{\hat{x}} = \frac{\tilde{u}_w(\hat{x})\hat{x}}{\nu},$$
$$Rb = \frac{\gamma^*\left(\hat{n}_w - \hat{n}_0\right)\left(\tilde{\rho}_m - \tilde{\rho}_f\right)}{\left(1 - \hat{C}_\infty\right)\left(\hat{T}_w - \hat{T}_0\right)}, \quad \delta = \frac{Q_0}{a\left(\widehat{\rho c_p}\right)_f}, \quad \Omega = \frac{\hat{n}_\infty}{\left(\hat{n}_w - \hat{n}_0\right)}, \quad B = \frac{e_2}{e_1}, E1 = \frac{\hat{E}_0}{\tilde{B}_0 a\nu_f}.$$

By replacing Eq. (12) in Eq. (7), the equivalent non-dimensional boundary conditions may be found, which are as follows:

$$\begin{cases} g(0) = 0, \\ f(0) = 0, \\ f'(0) = 1, \\ \theta(0) = 1 - S, \\ \phi(0) = 1 - Q, \\ \xi(0) = 1 - B, \end{cases} \quad at\ \eta = 0, \ \ and \quad \begin{cases} f'(\eta) \to 0, \\ g(\eta) \to 0, \\ \theta(\eta) \to 0, \\ \phi(\eta) \to 0, \\ \xi(\eta) \to 0, \end{cases} \quad as\ \ \eta \to \infty. \tag{19}$$

It is noted that the micropolar impacts are not accounted for in the nanofluidic model by omitting the vertex viscosity, i.e., $(K = 0)$.

III. MODELING ANNs WITH A SIGMOID FUNCTION

In several fields, the ANNs' capacity to employ the sigmoid activation function is used to produce results that are steady, consistent, and dependable. With backpropagation NNs, the EMHD-BCMN-TRS fluid mathematical model found in Eqs. (13)–(17) is expressed as follows, taking into account the derivatives in the input, hidden, and output layers:

$$\begin{aligned}
\begin{bmatrix} f, f', f'', \\ f''' \end{bmatrix} &= \begin{bmatrix} \sum_{i=1}^{s} \hbar_i L(\lambda_i \eta + \ell_i), \sum_{i=1}^{s} \hbar_i \frac{d}{d\eta} L(\lambda_i \eta + \ell_i), \sum_{i=1}^{s} \hbar_i \frac{d^2}{d\eta^2} L(\lambda_i \eta + \ell_i), \\ \sum_{i=1}^{s} \hbar_i \frac{d^3}{d\eta^3} L(\lambda_i \eta + \ell_i) \end{bmatrix} \\
[g, g', g''] &= \left[\sum_{i=1}^{s} \hbar_i L(\lambda_i \eta + \ell_i), \sum_{i=1}^{s} \hbar_i \frac{d}{d\eta} L(\lambda_i \eta + \ell_i), \sum_{i=1}^{s} \hbar_i \frac{d^2}{d\eta^2} L(\lambda_i \eta + \ell_i) \right] \\
[\theta, \theta', \theta''] &= \left[\sum_{i=1}^{s} \hbar_i L(\lambda_i \eta + \ell_i), \sum_{i=1}^{s} \hbar_i \frac{d}{d\eta} L(\lambda_i \eta + \ell_i), \sum_{i=1}^{s} \hbar_i \frac{d^2}{d\eta^2} L(\lambda_i \eta + \ell_i) \right] \\
[\phi, \phi', \phi''] &= \left[\sum_{i=1}^{s} \hbar_i L(\lambda_i \eta + \ell_i), \sum_{i=1}^{s} \hbar_i \frac{d}{d\eta} L(\lambda_i \eta + \ell_i), \sum_{i=1}^{s} \hbar_i \frac{d^2}{d\eta^2} L(\lambda_i \eta + \ell_i) \right] \\
[\Psi, \Psi', \Psi''] &= \left[\sum_{i=1}^{s} \hbar_i L(\lambda_i \eta + \ell_i), \sum_{i=1}^{s} \hbar_i \frac{d}{d\eta} L(\lambda_i \eta + \ell_i), \sum_{i=1}^{s} \hbar_i \frac{d^2}{d\eta^2} L(\lambda_i \eta + \ell_i) \right]
\end{aligned} \tag{20}$$

A sigmoid function is a restricted, differentiable real function with a single inflection point and a non-negative derivative, all referring to the same mathematical idea. A sigmoid function is illustrated by the formula $f(\eta) = \frac{1}{1+e^{-\eta}}$.

The sigmoid function $f(\lambda_i \eta + \ell_i) = \frac{1}{1+e^{\lambda_i \eta + \ell_i}}$ is employed in Eq. (20). Applying this function results in a new mathematical form,

$$\begin{aligned}
\begin{bmatrix} f, f', \\ f'', f''' \end{bmatrix} &= \begin{bmatrix} \sum_{i=1}^{s} \hbar_i \left(\frac{1}{1+e^{-(\lambda_i \eta + \ell_i)}} \right), \sum_{i=1}^{s} \hbar_i \lambda_i \left(\frac{e^{-(\lambda_i \eta + \ell_i)}}{1+e^{-(\lambda_i \eta + \ell_i)^2}} \right), \quad \sum_{i=1}^{s} \hbar_i \lambda_i^2 \left(\frac{2e^{-2(\lambda_i \eta + \ell_i)}}{1+e^{-(\lambda_i \eta + \ell_i)^3}} - \frac{e^{-(\lambda_i \eta + \ell_i)}}{1+e^{-(\lambda_i \eta + \ell_i)^2}} \right), \\ \sum_{i=1}^{s} \hbar_i \lambda_i^3 \left(\frac{6e^{-3(\lambda_i \eta + \ell_i)}}{1+e^{-(\lambda_i \eta + \ell_i)^4}} - \frac{6e^{-2(\lambda_i \eta + \ell_i)}}{1+e^{-(\lambda_i \eta + \ell_i)^3}} + \frac{e^{-(\lambda_i \eta + \ell_i)}}{1+e^{-(\lambda_i \eta + \ell_i)^2}} \right) \end{bmatrix} \\
\begin{bmatrix} g, g', \\ g'' \end{bmatrix} &= \left[\sum_{i=1}^{s} \hbar_i \left(\frac{1}{1+e^{-(\lambda_i \eta + \ell_i)}} \right), \sum_{i=1}^{s} \hbar_i \lambda_i \left(\frac{e^{-(\lambda_i \eta + \ell_i)}}{1+e^{-(\lambda_i \eta + \ell_i)^2}} \right), \sum_{i=1}^{s} \hbar_i \lambda_i^2 \left(\frac{2e^{-2(\lambda_i \eta + \ell_i)}}{1+e^{-(\lambda_i \eta + \ell_i)^3}} - \frac{e^{-(\lambda_i \eta + \ell_i)}}{1+e^{-(\lambda_i \eta + \ell_i)^2}} \right) \right] \\
\begin{bmatrix} \theta, \theta', \\ \theta'' \end{bmatrix} &= \left[\sum_{i=1}^{s} \hbar_i \left(\frac{1}{1+e^{-(\lambda_i \eta + \ell_i)}} \right), \sum_{i=1}^{k} \hbar_i \lambda_i \left(\frac{e^{-(\lambda_i \eta + \ell_i)}}{1+e^{-(\lambda_i \eta + \ell_i)^2}} \right), \sum_{i=1}^{s} \hbar_i \lambda_i^2 \left(\frac{2e^{-2(\lambda_i \eta + \ell_i)}}{1+e^{-(\lambda_i \eta + \ell_i)^3}} - \frac{e^{-(\lambda_i \eta + \ell_i)}}{1+e^{-(\lambda_i \eta + \ell_i)^2}} \right) \right] \\
\begin{bmatrix} \phi, \phi', \\ \phi'' \end{bmatrix} &= \left[\sum_{i=1}^{s} \hbar_i \left(\frac{1}{1+e^{-(\lambda_i \eta + \ell_i)}} \right), \sum_{i=1}^{s} \hbar_i \lambda_i \left(\frac{e^{-(\lambda_i \eta + \ell_i)}}{1+e^{-(\lambda_i \eta + \ell_i)^2}} \right), \sum_{i=1}^{s} \hbar_i \lambda_i^2 \left(\frac{2e^{-2(\lambda_i \eta + \ell_i)}}{1+e^{-(\lambda_i \eta + \ell_i)^3}} - \frac{e^{-(\lambda_i \eta + \ell_i)}}{1+e^{-(\lambda_i \eta + \ell_i)^2}} \right) \right] \\
\begin{bmatrix} \Psi, \Psi', \\ \Psi'' \end{bmatrix} &= \left[\sum_{i=1}^{s} \hbar_i \left(\frac{1}{1+e^{-(\lambda_i \eta + \ell_i)}} \right), \sum_{i=1}^{s} \hbar_i \lambda_i \left(\frac{e^{-(\lambda_i \eta + \ell_i)}}{1+e^{-(\lambda_i \eta + \ell_i)^2}} \right), \quad \sum_{i=1}^{s} \hbar_i \lambda_i^2 \left(\frac{2e^{-2(\lambda_i \eta + \ell_i)}}{1+e^{-(\lambda_i \eta + \ell_i)^3}} - \frac{e^{-(\lambda_i \eta + \ell_i)}}{1+e^{-(\lambda_i \eta + \ell_i)^2}} \right) \right]
\end{aligned} \tag{21}$$

In the above-mentioned network, s represents the neurons, $W = [\hbar_i, \lambda_i, \ell_i]$ is the unknown weight vector, i.e., $\hbar_i = [\hbar_1, \hbar_2, \ldots, \hbar_k], \lambda_i = [\lambda_1, \lambda_2, \ldots, \lambda_k]$, and $\ell_i = [\ell_1, \ell_2, \ldots, \ell_k]$.

Equation (21) introduces the sigmoid function $f(\lambda_i \eta + \ell_{ii}) = \frac{1}{1+e^{\lambda_i \eta + \ell_i}}$ as the objective function and its higher derivatives i.e., third order. Furthermore, these equations include the sigmoid function. Equation (20) denotes the function $f(\eta)$ and its first, second, and third order derivatives. Equation (21) denotes the same function $f(\eta)$ and its derivatives after applying the sigmoid function. In the same way, Eq. (20) represents the functions $g(\eta)$, $\theta(\eta)$, $\phi(\eta)$, and $\Psi(\eta)$ along with their first and second order derivatives. On the other hand, Eq. (21) represents the functions $g(\eta)$, $\theta(\eta)$, $\phi(\eta)$, and $\Psi(\eta)$ and their derivatives up to second order, after merging the sigmoid function.

IV. FORMULATION OF THE FITNESS FUNCTION

Equation (22) in our modeling uses the mean squared error (MSE) as the objective function,

$$\varepsilon = \varepsilon_1 + \varepsilon_2 + \varepsilon_3 + \varepsilon_4 + \varepsilon_5, \tag{22}$$

$$\begin{aligned}
\varepsilon_1 &= \frac{1}{s}\sum_{i=1}^{s}\left((1+K)f''' - f'^2 - Mf' + M\hat{E} + ff'' + Kg' + \lambda(\theta + Nr\phi - Rb\Psi)\right)^2,\\
\varepsilon_2 &= \frac{1}{s}\sum_{i=1}^{s}\left(\left(1+\frac{K}{2}\right)g'' - K\left(f'' + 2g\right) - f'g + fg'\right)^2,\\
\varepsilon_3 &= \frac{1}{s}\sum_{i=1}^{s}\left(\begin{array}{c}\left(1+\frac{4}{3}Rd\right)\theta'' + \Pr f\theta' + \Pr\left(Nb\theta'\phi' + Nt\theta'^2\right) - \Pr\left(f'\theta + Sf'\right) + \Pr\delta\theta\\ +M^2 Ec\left(f'^2 + \hat{E}^2 - 2\hat{E}f'\right)\end{array}\right)^2,\\
\varepsilon_4 &= \frac{1}{s}\sum_{i=1}^{s}\left(\phi'' + (Nt/Nb)\theta'' + Sc\left(f\phi' - f'\phi - Qf'\right)\right)^2,\\
\varepsilon_5 &= \frac{1}{s}\sum_{i=1}^{s}\left(\Psi'' - Lb\left(\Psi f' + Bf' - \Psi' f\right) - Pe(\Psi+\Omega)\phi'' - Pe\Psi'\phi'\right)^2.
\end{aligned} \tag{23}$$

This objective function is represented by Eq. (22), where ε is the mean of squared error (MSE), which is the summation of ε_1, ε_2, ε_3, ε_4, and ε_5. Equation (23) presents the expressions for ε_1, ε_2, ε_3, ε_4, and ε_5. The following five equations show the MSE, while the coefficient of determination (R) is expressed as

$$R = \sqrt{1 - \frac{\sum_{i=1}^{s}\left(X_{\exp(i)} - X_{ANN(i)}\right)^2}{\sum_{i=1}^{N}\left(X_{\exp(i)}\right)^2}}. \tag{24}$$

Furthermore, an additional critical parameter used in ANN models' efficiency scores is the discrepancy between the error and the projected dataset. For each of the five single layer network, the error rates (%) between the target and forecast data were determined, and their dependability was evaluated,

$$\text{Error rate}(\%) = \left[\frac{X_{\exp} - X_{ANN}}{X_{\exp}}\right] \times 100. \tag{25}$$

With the availability of ANN-LMBOA weights, one must optimize ϵ, the objective function, so that $\epsilon \to 0$ in order to solve the EMHD-BCMN-TRS fluid model, based on the previous necessity of the training datapoints, testing datapoints, and validation datapoints as required in classically supervised neural networks, trained via an appropriate optimization method (ANN-LMBOA method).

V. DATASET FORMATION FOR PROPOSED SOLUTIONS

One of the many applications of artificial intelligence (AI) is artificial neural networks (ANNs). Because ANNs can simulate nonlinear phenomena and are adaptable to them, they have been used in a variety of applications. ANNs are helpful in a variety of sectors because they can adapt and learn from the data they are given. Numerous fields benefit from the application of ANNs, such as machine translation, email spam filtering, quantum chemistry, natural resource management, sequence recognition, system identification, process control, sensor data analysis, and financial analysis. ANNs and other machine learning methods can be used to model complex data associations. They can therefore be used for a variety of purposes, including the ones already stated. Therefore, the ANN-LMBOA stochastic numerical based approach based on backpropagation is more dependable. Gradient descent is a supervised learning technique called backpropagation, which reduces the slope of the error curve and minimizes error.

To train the ANN-LMBOA algorithm to handle a fluid problem, pertinent data must be gathered and organized in a dataset for suggested solutions. This dataset is used as the basis for training and assessing the effectiveness of several algorithms, including ANNs. It takes considerable consideration to choose representative samples, prepare the data, and ensure their quality and dependability. In order for the model to generate reliable results and generalize, the composition and diversity of the dataset are crucial. Therefore, the

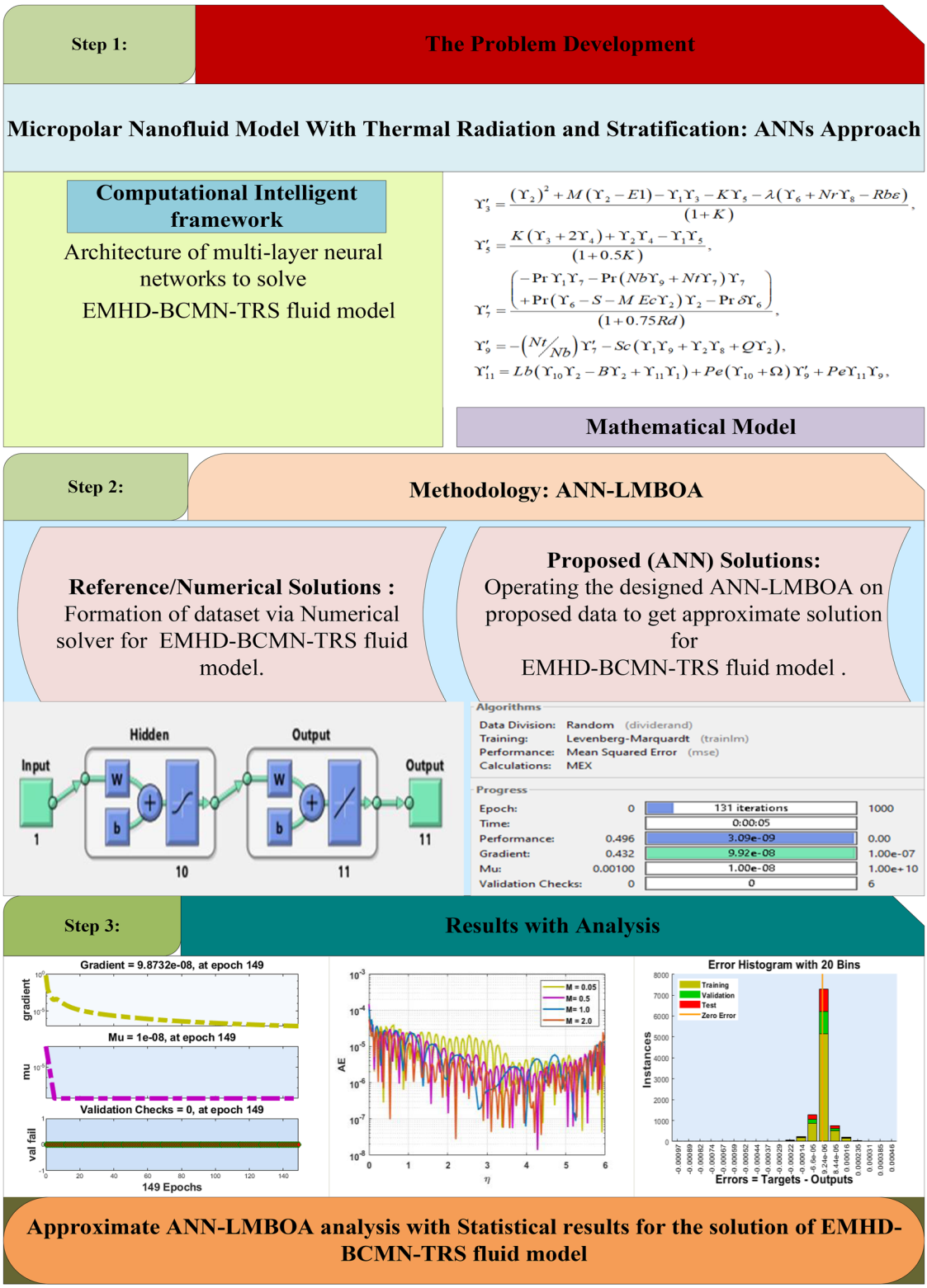

FIG. 2. ANN-LMBOA scheme for the EMHD-BCMN-TRS flow model.

first step in deploying neural networks to give effective answers is to create a well-constructed dataset.

The following three sections include the formation and methodologies for solving the nonlinear EMHD-BCMN-TRS fluid model.

The nonlinear EMHD-BCMN-TRS fluid model has four classes, velocity $(f'(\eta))$, angular velocity $(g(\eta))$, temperature $(\theta(\eta))$, and concentration $(\phi(\eta))$, and each class consists of two cases.

In order to construct the dataset from differential equations [Eqs. (13)–(17)], the initial phase furnishes the data required by the solution i.e., bvp4c, which adds the boundary conditions [Eq. (19)] and transforms higher order nonlinear ODEs into first order ODEs. A built-in ANN-LMBOA computing platform with network modeling, layer structure, and the backpropagation mechanism is provided in the second section. The last step offers guidance on how to solve the nonlinear EMHD-BCMN-TRS fluid model using the suggested ANN-LMBOA.

The "bvp4c solver" routine for solving ODEs in the MATLAB software package is used to calculate the reference datasets for the various classes of the nonlinear system of the EMHD-BCMN-TRS fluid model, which are characterized by five case-based systems of ODEs [Eqs. (30)–(34)], as shown in the set of equations in Eqs. (13)–(17). Tolerance, good accuracy, stoppage conditions, and other default parameter settings are used when the "bvp4c solver" operation is run. The dataset collected is used to model the networks with different data distributions in the training data, testing execution of data, and validation of results for the provided samples of each instance (cases 1 through 5) in the nonlinear system of the EMHD-BCMN-TRS fluid model [Eqs. (13)–(17)].

The suggested framework for the ANN-LMBOA methodology is depicted in Fig. 2, along with performance analysis and optimization techniques for the problem, outcome description, and layer structure. These higher order ODEs have been transformed by assuming

$$\begin{aligned} f''(\eta) = \Upsilon_3,\ f'(\eta) = \Upsilon_2,\ f(\eta) = \Upsilon_1,\\ g'(\eta) = \Upsilon_5, \qquad g(\eta) = \Upsilon_4,\\ \theta(\eta) = \Upsilon_6, \qquad \theta'(\eta) = \Upsilon_7,\\ \phi(\eta) = \Upsilon_8, \qquad \phi'(\eta) = \Upsilon_9,\\ \xi(\eta) = \Upsilon_{10}, \qquad \xi'(\eta) = \Upsilon_{11}, \end{aligned} \tag{26}$$

$$\begin{aligned} \Upsilon_3' &= \frac{1}{(1+K)}\Big({\Upsilon_2}^2 + M\Upsilon_2 - M\widehat{E} - \Upsilon_1\Upsilon_3 - K\Upsilon_5\\ &\quad - \lambda(\Upsilon_6 + Nr\Upsilon_8 - Rb\Upsilon_{10})\Big),\\ \Upsilon_5' &= \frac{(K(\Upsilon_3 + 2\Upsilon_4) + \Upsilon_2\Upsilon_4 - \Upsilon_1\Upsilon_5)}{\left(1 + \frac{K}{2}\right)},\\ \Upsilon_7' &= \frac{\left(\begin{array}{c}\Pr(\Upsilon_2\Upsilon_6 + S\Upsilon_2) + \Pr\delta\Upsilon_6 - \Pr\Upsilon_1\Upsilon_7\\ -\Pr\left(Nb\Upsilon_7\Upsilon_9 + Nt{\Upsilon_7}^2\right) - M^2 Ec\left({\Upsilon_2}^2 + \widehat{E}^2 - 2\widehat{E}\Upsilon_2\right)\end{array}\right)}{\left(1 + \frac{4}{3}Rd\right)},\\ \Upsilon_9' &= -(Nt/Nb)\Upsilon_7' - Sc(\Upsilon_1\Upsilon_9 - \Upsilon_2\Upsilon_8 - Q\Upsilon_2),\\ \Upsilon_{11}' &= Lb(\Psi\Upsilon_2 + B\Upsilon_2 - \Upsilon_{11}\Upsilon_1) + Pe(\Upsilon_{10} + \Omega)\Upsilon_9' + Pe\Upsilon_9\Upsilon_{11}. \end{aligned} \tag{27}$$

The bvp4c approach with suitable boundary conditions is

$$\begin{aligned} &\Upsilon_a(10) = 1 - B, \quad \Upsilon_a(8) = 1 - Q, \quad \Upsilon_a(6) = 1 - S,\\ &\Upsilon_a(4) = 0, \quad \Upsilon_a(2) = 1, \quad \Upsilon_a(1) = 0, \quad \Upsilon_b(10) = 0,\\ &\Upsilon_b(8) = 0, \quad \Upsilon_b(6) = 0, \quad \Upsilon_b(4) = 0, \quad \Upsilon_b(2) = 0. \end{aligned} \tag{28}$$

Taking both into account, we have

$$f'''(\eta) = \Upsilon_3',\ g''(\eta) = \Upsilon_5',\ \theta''(\eta) = \Upsilon_7',\ \phi''(\eta) = \Upsilon_9',\ \Psi''(\eta) = \Upsilon_{11}'. \tag{29}$$

VI. PROPOSED METHODOLOGY: LMBOA

The numerical computing stochastic procedure for the EMHD-BCMN-TRS fluid model is provided in the following two consecutive phases:

- Detailed and thorough explanations are provided for the ANN-LMBOA based numerical computing stochastic process.
- The EMHD-BCMN-TRS fluid model's computing stochastic numerical technique can be carried out with the support of the implementation procedures.

Figure 1 illustrates a suitable framework for the design process flow using the EMHD-BCMN-TRS fluid model's stochastic numerical approach. Figure 3 shows the multi-layer architecture that drives the ANN-LMBOA. With a particular layer layout, the architecture is implemented in "MATLAB" and consists of single input-hidden-output layers with ten neurons. Many functions are used in the

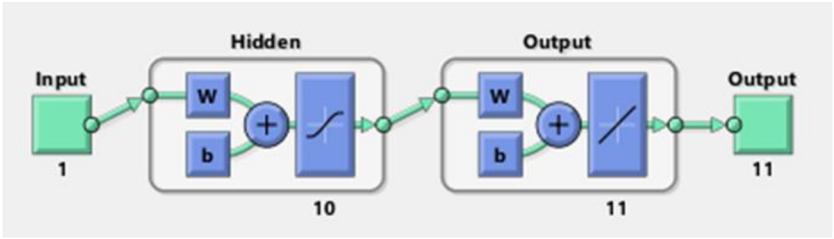

FIG. 3. Stochastic architecture of the EMHD-BCMN-TRS fluid model.

TABLE I. ANN-LMBOA method parameter modification.

Index	Settings
Minimum values of the gradient	10^{-6}
Increasing mu values	10
Fitness values (MSE)	0
Decreasing mu attributes	0.1
Validation features	15%
Sample selection	Manually/randomly
Flexible parameter, i.e., mu	1×10^{-10}
Training features	70%
Maximum epochs	1000
Maximum mu capabilities	10^{9}
Testing features	15%
Stoppage criteria	By default
Generated dataset	bvp4c solver
Hidden neurons	≈10 − 15
Layers (hidden, input, and output)	Single

training process, including the ANN-LMBOA, a log-sigmoid activation function, 1000 epochs, and n-fold cross validation. Default parameters for tolerance, stoppage limits, step size, and iteration are used throughout the training phase. The input and target values that make up the labeled data are obtained from a conventional numerical solution. In order to make training easier, 80% of the data that are randomly selected are used for training of the obtained data, with 10% going toward testing the execution of data and 10% toward validation of the results.

Based on the current related research, a design with ten neurons is chosen to guarantee a neural network model that is balanced between overfitting data and underfitting data through the training of the obtained data and validation of the results.[51–56] This choice aims to avoid issues such as the premature convergence linked to underfitting and the overfitting problem, which arises when utilizing more neurons than 10. Overfitting can lead to greater complexity without significantly improving accuracy. The training features, testing features, and validation features for the ANN-LMBOA procedure are randomly chosen, with proportions of 70%, 15%, and 15%, respectively.

It is crucial to keep in mind that using fewer training samples (e.g., 30%–50%) raises the mean square error (MSE) during testing, which degrades the algorithm's performance overall. Conversely, modestly increasing the number of training samples (e.g., 90%) while decreasing the proportions allotted to data testing and result validation (e.g., 5% each) improves the algorithm's precision for labeled data (bias input and targets). Nonetheless, the resilience of the system is validated using a restricted set of objective data that is acquired without being aware of the targets beforehand. The execution of the ANN-LMBOA procedure for solving the EMHD-BCMN-TRS fluid model together with the parameter setting is given in Table I.

VII. NUMERICAL RESULTS SIMULATIONS WITH INTERPRETATION

Four ANN-LMBOA-implemented classes of the EMHD-BCMN-TRS fluid model are provided in this section. Each of the eight variants' mathematical descriptions is given in the following cases:

Case 1: Velocity distribution: Consider the EMHD-BCMN-TRS fluid model with $Sc = 0.2$, $Nt = 0.1$, $K = 0.2$, $Nr = 0.1$, $Rd = 1.0$, $Pe = 1.2$, $Nb = 0.1$, $Ec = 0.02$, $\lambda 1 = 0.1$, $S = 0.1$, $\lambda = 0.1$, $B = 0.1$, $\Pr = 1.2$, $M = 0.05$, $Lb = 1.2$, $Q = 0.1$, $Rb = 0.1$, $\delta = 0.5$, $\Omega = 0.2$, $E1 = 0.5$, and $Nr = 0.3$ using four different velocity distribution numerical values $(M \text{ and } E1)$ to acquire the numerical results,

$$\begin{gathered}
\Upsilon_3' = \frac{(\Upsilon_2)^2 + M(\Upsilon_2 - E1) - \Upsilon_1\Upsilon_3 - K\Upsilon_5 - \lambda(\Upsilon_6 + Nr\Upsilon_8 - Rb\varepsilon)}{(1+K)}, \\
\Upsilon_3(0) = 6, \\
\Upsilon_5' = \frac{K(\Upsilon_3 + 2\Upsilon_4) + \Upsilon_2\Upsilon_4 - \Upsilon_1\Upsilon_5}{(1+0.5K)}, \Upsilon_5(0) = 6, \\
\Upsilon_7' = \frac{\begin{pmatrix} -\Pr\Upsilon_1\Upsilon_7 - \Pr(Nb\Upsilon_9 + Nt\Upsilon_7)\Upsilon_7 \\ +\Pr(\Upsilon_6 - S - M\,Ec\Upsilon_2)\Upsilon_2 - \Pr\delta\Upsilon_6 \end{pmatrix}}{(1+0.75Rd)}, \Upsilon_7(0) = 6, \\
\Upsilon_9' = -(Nt/Nb)\Upsilon_7' - Sc(\Upsilon_1\Upsilon_9 + \Upsilon_2\Upsilon_8 + Q\Upsilon_2), \Upsilon_9(0) = 6, \\
\Upsilon_{11}' = Lb(\Upsilon_{10}\Upsilon_2 - B\Upsilon_2 + \Upsilon_{11}\Upsilon_1) + Pe(\Upsilon_{10} + \Omega)\Upsilon_9' \\
+Pe\Upsilon_{11}\Upsilon_9, \Upsilon_{11}(0) = 6.
\end{gathered} \tag{30}$$

Case 2: Angular velocity distribution: Consider the EMHD-BCMN-TRS fluid model with $Sc = 0.2$, $Nt = 0.1$, $K = 0.2$, $Nr = 0.1$, $Rd = 1.0$, $Pe = 1.2$, $Nb = 0.1$, $Ec = 0.02$, $\lambda_1 = 0.1$, $S = 0.1$, $\lambda = 0.1$, $B = 0.1$, $\Pr = 1.2$, $M = 0.05$, $Lb = 1.2$, $Q = 0.1$, $Rb = 0.1$, $\delta = 0.5$, $E1 = 0.5$, $\Omega = 0.2$, and $Nr = 0.3$ using four different angular velocity distribution numerical values $(M \text{ and } K)$ to acquire the numerical results,

$$\begin{gathered}
\Upsilon_3' = \frac{(\Upsilon_2)^2 + M(\Upsilon_2 - E1) - \Upsilon_1\Upsilon_3 - K\Upsilon_5 - \lambda(\Upsilon_6 + Nr\Upsilon_8 - Rb\varepsilon)}{(1+K)}, \\
\Upsilon_3(0) = 10, \\
\Upsilon_5' = \frac{K(\Upsilon_3 + 2\Upsilon_4) + \Upsilon_2\Upsilon_4 - \Upsilon_1\Upsilon_5}{(1+0.5K)}, \Upsilon_5(0) = 10, \\
\Upsilon_7' = \frac{\begin{pmatrix} -\Pr\Upsilon_1\Upsilon_7 - \Pr(Nb\Upsilon_9 + Nt\Upsilon_7)\Upsilon_7 \\ +\Pr(\Upsilon_6 - S - M\,Ec\Upsilon_2)\Upsilon_2 - \Pr\delta\Upsilon_6 \end{pmatrix}}{(1+0.75Rd)}, \Upsilon_7(0) = 10, \\
\Upsilon_9' = -(Nt/Nb)\Upsilon_7' - Sc(\Upsilon_1\Upsilon_9 + \Upsilon_2\Upsilon_8 + Q\Upsilon_2), \Upsilon_9(0) = 10, \\
\Upsilon_{11}' = Lb(\Upsilon_{10}\Upsilon_2 - B\Upsilon_2 + \Upsilon_{11}\Upsilon_1) + Pe(\Upsilon_{10} + \Omega)\Upsilon_9' \\
+Pe\Upsilon_{11}\Upsilon_9, \Upsilon_{11}(0) = 10.
\end{gathered} \tag{31}$$

Case 3: Temperature distribution: Consider the EMHD-BCMN-TRS fluid model with $Sc = 0.2$, $Nt = 0.1$, $K = 0.2$, $Nr = 0.1$, $Rd = 1.0$, $Pe = 1.2$, $Nb = 0.1$, $Ec = 0.02$, $\lambda_1 = 0.1$, $S = 0.1$, $\lambda = 0.1$, $B = 0.1$, $\Pr = 1.2$, $M = 0.05$, $Lb = 1.2$, $Q = 0.1$, $Rb = 0.1$, $\delta = 0.5$, $\Omega = 0.2$, $E1 = 0.5$, and $Nr = 0.3$ using four different temperature distribution numerical values $(Rd \text{ and } S)$ to acquire the numerical results,

$$\Upsilon_3' = \frac{(\Upsilon_2)^2 + M(\Upsilon_2 - E1) - \Upsilon_1\Upsilon_3 - K\Upsilon_5 - \lambda(\Upsilon_6 + Nr\Upsilon_8 - Rb\varepsilon)}{(1+K)},$$
$$\Upsilon_3(0) = 10,$$
$$\Upsilon_5' = \frac{K(\Upsilon_3 + 2\Upsilon_4) + \Upsilon_2\Upsilon_4 - \Upsilon_1\Upsilon_5}{(1+0.5K)}, \Upsilon_5(0) = 10,$$
$$\Upsilon_7' = \frac{\begin{pmatrix} -\Pr\Upsilon_1\Upsilon_7 - \Pr(Nb\Upsilon_9 + Nt\Upsilon_7)\Upsilon_7 \\ +\Pr(\Upsilon_6 - S - M\,Ec\Upsilon_2)\Upsilon_2 - \Pr\delta\Upsilon_6 \end{pmatrix}}{(1+0.75Rd)}, \Upsilon_7(0) = 10, \quad (32)$$
$$\Upsilon_9' = -(Nt/Nb)\Upsilon_7' - Sc(\Upsilon_1\Upsilon_9 + \Upsilon_2\Upsilon_8 + Q\Upsilon_2), \Upsilon_9(0) = 10,$$
$$\Upsilon_{11}' = Lb(\Upsilon_{10}\Upsilon_2 - B\Upsilon_2 + \Upsilon_{11}\Upsilon_1) + Pe(\Upsilon_{10} + \Omega)\Upsilon_9' + Pe\Upsilon_{11}\Upsilon_9, \Upsilon_{11}(0) = 10.$$

Case 4: Concentration distribution: Consider the EMHD-BCMN-TRS fluid model with $Sc = 0.2$, $Nt = 0.1$, $K = 0.2$, $Nr = 0.1$, $Rd = 1.0$, $Pe = 1.2$, $Nb = 0.1$, $Ec = 0.02$, $\lambda_1 = 0.1$, $S = 0.1$, $\lambda = 0.1$, $B = 0.1$, $\Pr = 1.2$, $M = 0.05$, $Lb = 1.2$, $Q = 0.1$, $Rb = 0.1$, $\delta = 0.5$, $\Omega = 0.2$, $E1 = 0.5$, and $Nr = 0.3$ using four different concentration distribution numerical values (Sc *and* Q) to acquire the numerical results,

$$\Upsilon_3' = \frac{(\Upsilon_2)^2 + M(\Upsilon_2 - E1) - \Upsilon_1\Upsilon_3 - K\Upsilon_5 - \lambda(\Upsilon_6 + Nr\Upsilon_8 - Rb\varepsilon)}{(1+K)},$$
$$\Upsilon_3(0) = 20,$$
$$\Upsilon_5' = \frac{K(\Upsilon_3 + 2\Upsilon_4) + \Upsilon_2\Upsilon_4 - \Upsilon_1\Upsilon_5}{(1+0.5K)}, \Upsilon_5(0) = 20,$$
$$\Upsilon_7' = \frac{\begin{pmatrix} -\Pr\Upsilon_1\Upsilon_7 - \Pr(Nb\Upsilon_9 + Nt\Upsilon_7)\Upsilon_7 \\ +\Pr(\Upsilon_6 - S - M\,Ec\Upsilon_2)\Upsilon_2 - \Pr\delta\Upsilon_6 \end{pmatrix}}{(1+0.75Rd)}, \Upsilon_7(0) = 20, \quad (33)$$
$$\Upsilon_9' = -(Nt/Nb)\Upsilon_7' - Sc(\Upsilon_1\Upsilon_9 + \Upsilon_2\Upsilon_8 + Q\Upsilon_2), \Upsilon_9(0) = 20,$$
$$\Upsilon_{11}' = Lb(\Upsilon_{10}\Upsilon_2 - B\Upsilon_2 + \Upsilon_{11}\Upsilon_1) + Pe(\Upsilon_{10} + \Omega)\Upsilon_9' + Pe\Upsilon_{11}\Upsilon_9, \Upsilon_{11}(0) = 20.$$

Case 5: Motile micro-organism distribution: Consider the EMHD-BCMN-TRS fluid model with $Sc = 0.2$, $Nt = 0.1$, $K = 0.2$, $Nr = 0.1$, $Rd = 1.0$, $Pe = 1.2$, $Nb = 0.1$, $Ec = 0.02$, $\lambda_1 = 0.1$, $S = 0.1$, $\lambda = 0.1$, $B = 0.1$, $\Pr = 1.2$, $M = 0.05$, $Lb = 1.2$, $Q = 0.1$, $Rb = 0.1$, $\delta = 0.5$, $\Omega = 0.2$, and $E1 = 0.5$ using four different motile micro-organism distribution numerical values (Q *and* Pe) to acquire the numerical results,

$$\Upsilon_3' = \frac{(\Upsilon_2)^2 + M(\Upsilon_2 - E1) - \Upsilon_1\Upsilon_3 - K\Upsilon_5 - \lambda(\Upsilon_6 + Nr\Upsilon_8 - Rb\varepsilon)}{(1+K)},$$
$$\Upsilon_3(0) = 7,$$
$$\Upsilon_5' = \frac{K(\Upsilon_3 + 2\Upsilon_4) + \Upsilon_2\Upsilon_4 - \Upsilon_1\Upsilon_5}{(1+0.5K)}, \Upsilon_5(0) = 7,$$
$$\Upsilon_7' = \frac{\begin{pmatrix} -\Pr\Upsilon_1\Upsilon_7 - \Pr(Nb\Upsilon_9 + Nt\Upsilon_7)\Upsilon_7 \\ +\Pr(\Upsilon_6 - S - M\,Ec\Upsilon_2)\Upsilon_2 - \Pr\delta\Upsilon_6 \end{pmatrix}}{(1+0.75Rd)}, \Upsilon_7(0) = 7, \quad (34)$$
$$\Upsilon_9' = -(Nt/Nb)\Upsilon_7' - Sc(\Upsilon_1\Upsilon_9 + \Upsilon_2\Upsilon_8 + Q\Upsilon_2), \Upsilon_9(0) = 7,$$
$$\Upsilon_{11}' = Lb(\Upsilon_{10}\Upsilon_2 - B\Upsilon_2 + \Upsilon_{11}\Upsilon_1) + Pe(\Upsilon_{10} + \Omega)\Upsilon_9' + Pe\Upsilon_{11}\Upsilon_9, \Upsilon_{11}(0) = 7.$$

The numerical interpretations are provided for the EMHD-BCMN-TRS fluid model in an input span of [0, 30]. The "nftool," a neural fitting command in MATLAB, is applied to solve the EMHD-BCMN-TRS fluid model using ≈10–15 ten neurons by selecting 70% for training features and 15% for both validation features and testing features. The obtained results for the EMHD-BCMN-TRS fluid model are plotted in Fig. 3.

Figures 4–8 show the graphs of the estimated outcomes for the EMHD-BCMN-TRS fluid model. The EMHD-BCMN-TRS fluid model's competent processes for each of the four parameter modifications are developed as shown in Fig. 4 using the states of performances with different attributes. The calculated MSE measures for training, authentication, best curve fitting, and testing features are provided in Fig. 4 (case1–case5), while the state transitions are plotted in Fig. 5 (case1–case5) to solve the EMHD-BCMN-TRS fluid model. The fluid model's optimal performance results are displayed at epochs of 149, 304, 530, 396, and 129, which lie around 3.9113×10^{-9}, 2.5601×10^{-9}, 1.3123×10^{-9}, 1.9625×10^{-9}, and 5.5426×10^{-9}, respectively, for all cases. The gradient values for the EMHD-BCMN-TRS fluid model are 9.8732×10^{-8}, 9.9168×10^{-8}, 9.966×10^{-8}, 9.9012×10^{-8}, and 9.8664×10^{-8}, respectively, for all cases. These graphical displays show how the EMHD-BCMN-TRS fluid model converges and is accurate. Figure 6 shows the plotting of the fitting curves (case1–case5) for each EMHD-BCMN-TRS fluid model, which shows the comparison of the obtained and reference results. Figure 7 (case1–case5) is drawn on the basis of EHs to solve the EMHD-BCMN-TRS fluid model using the ANN-LMBOA. It is observed that the EH values for case1–case5 lie around -6.6×10^{-5}, 2.69×10^{-5}, 6.46×10^{-6}, -1.2×10^{-5}, and 1.4×10^{-5}, respectively, for all cases. The correlation measurement plots are depicted in Fig. 8 (case1–case5), which indicates the regression features. The correlation features in terms of the coefficient of determination, i.e., values of R^2, lie around 1 to solve the EMHD-BCMN-TRS fluid model. These best plots of training attributes, testing attributes, and validation features indicate the accuracy of the scheme. The MSE-based convergence scheme based on the training attributes, epoch-time, authentication features, testing attributes, backpropagation measurements, and complexity is shown in Tables II–VI to solve the EMHD-BCMN-TRS fluid model. In Tables II–VI, the numerical values of the training parameter are used in order to minimize the error between the expected and actual outputs, and the neural network must be trained. Also Tables III, IV, and V show the results for cases 2, 3, and 4 respectively. This is carried out by putting the input data into the network and iteratively modifying the network's weights. The objective is to enable the network to learn from the data in order to produce precise classifications or predictions. The numerical values of the testing parameter in Tables II–VI are used for different datasets that the neural network has never seen before and are used to assess the network after it has been trained. This aids in evaluating the model's ability to generalize to fresh, untested data. The numerical values of the validation parameter exemplified in Tables II–VI for a subset of the data that is not used for training are set aside for validation during the training phase. The validation dataset aids in avoiding overfitting and fine-tuning hyperparameters. When a model works well on training data but not well on fresh data, this is known as overfitting. The neural network model's performance on a fluid model is listed in Tables II–VI. Depending on the particular values, it can

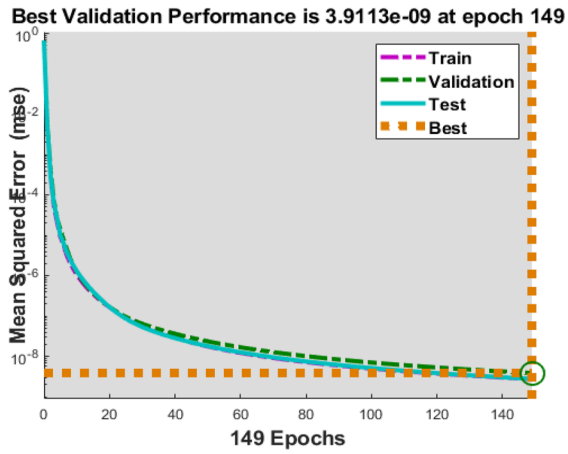

Case-1

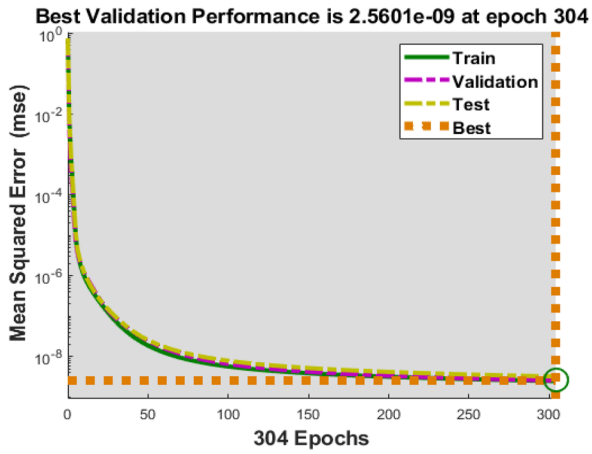

Case-2

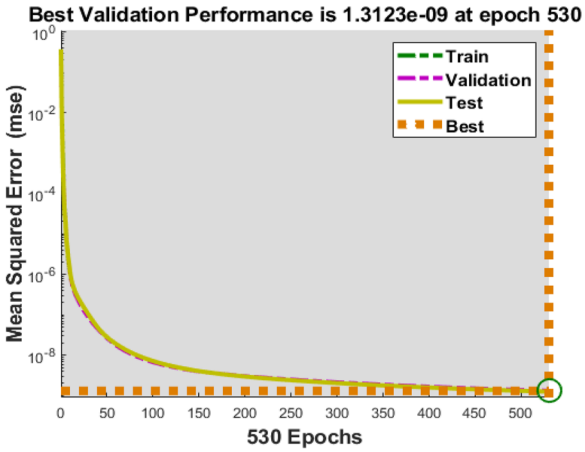

Case-3

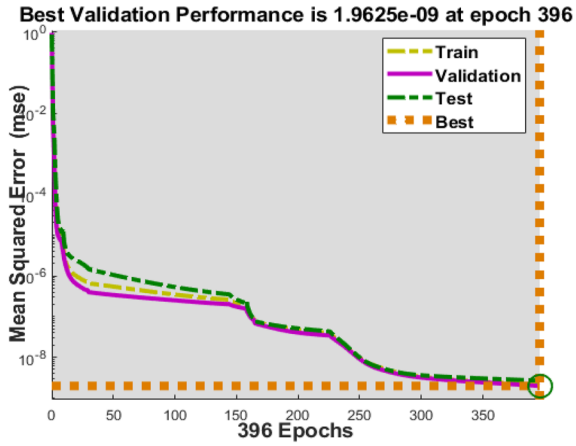

Case-4

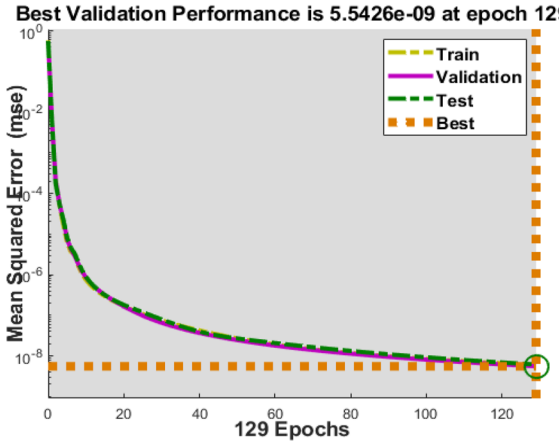

Case-5

FIG. 4. MSE for the ANN-LMBOA to solve the EMHD-BCMN-TRS fluid model for case-1 to case-5.

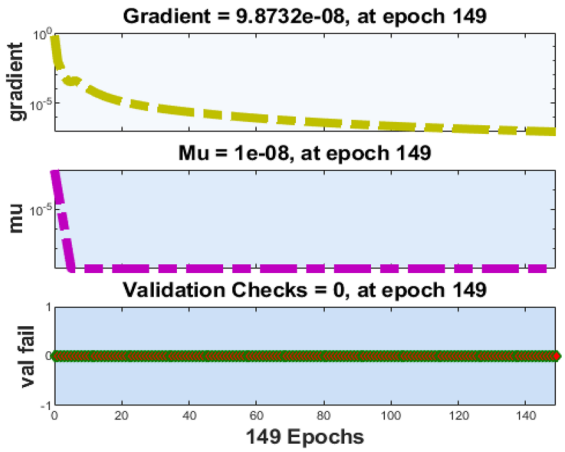

Case-1

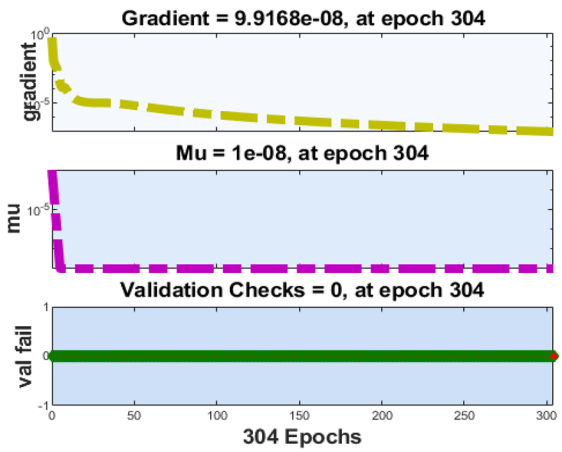

Case-2

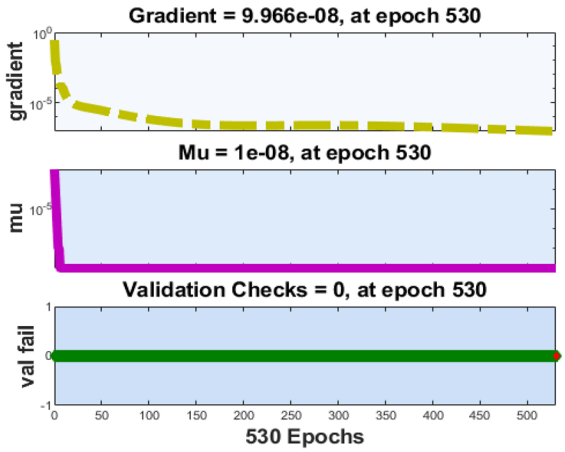

Case-3

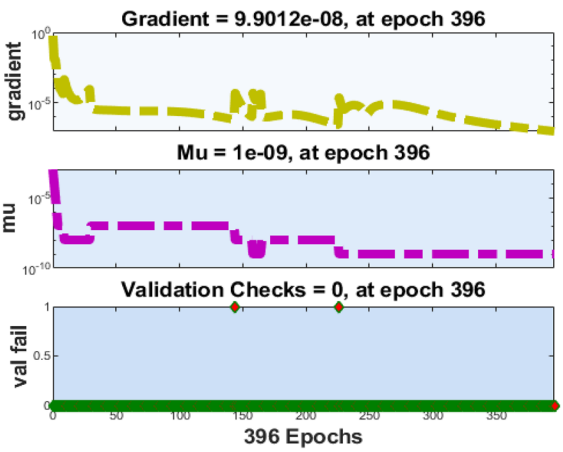

Case-4

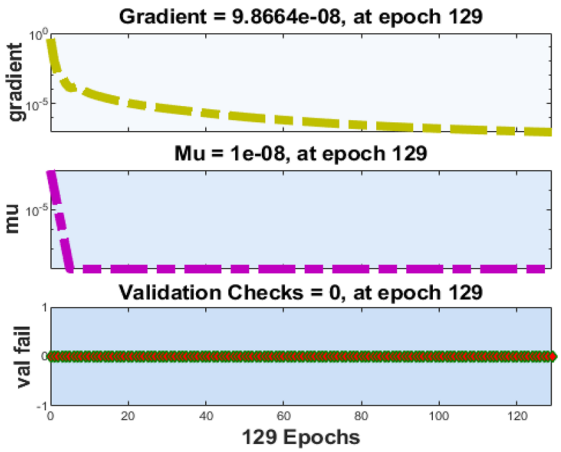

Case-5

FIG. 5. State transitions for the ANN-LMBOA to solve the EMHD-BCMN-TRS fluid model for case-1 to case-5.

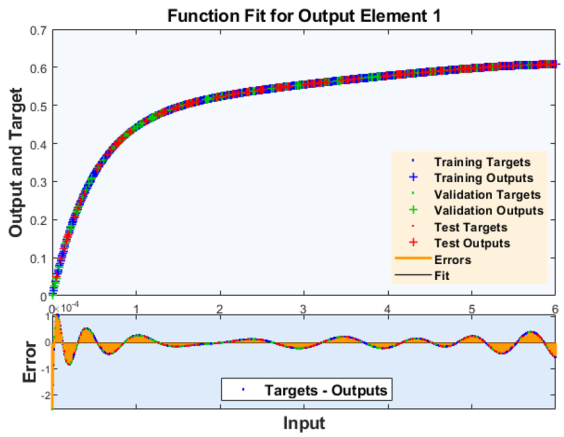

Case-1

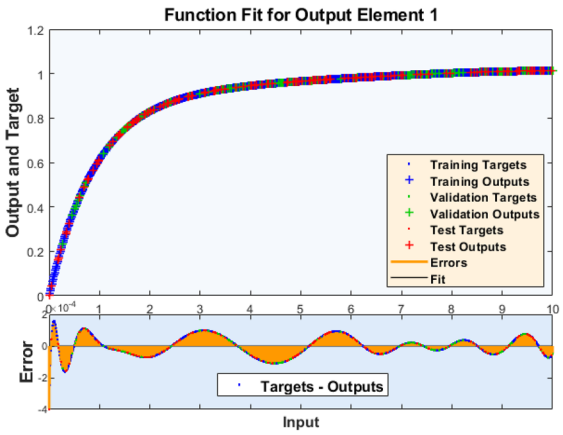

Case-2

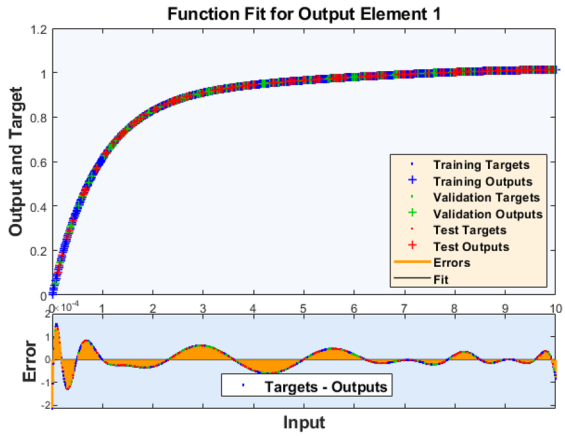

Case-3

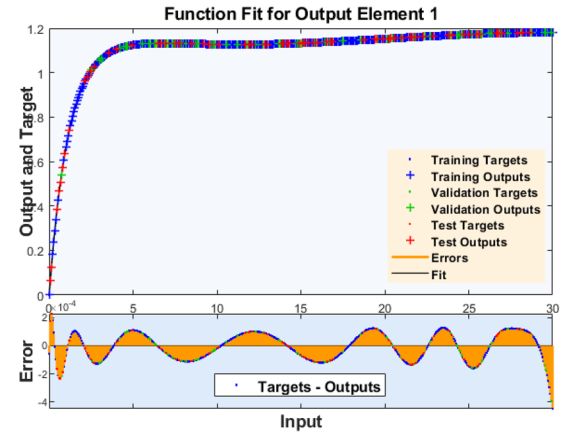

Case-4

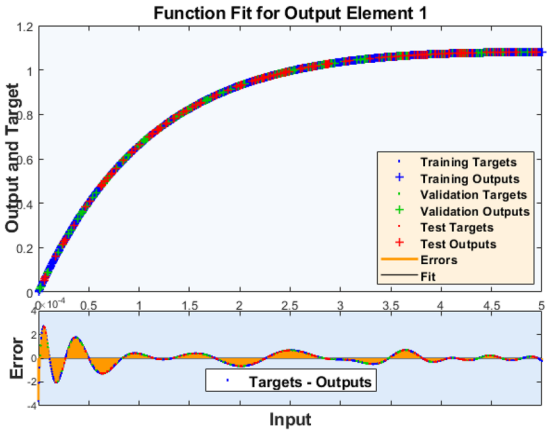

Case-5

FIG. 6. Comparison using ANN-LMBOA to solve the EMHD-BCMN-TRS fluid model for case-1 to case-5.

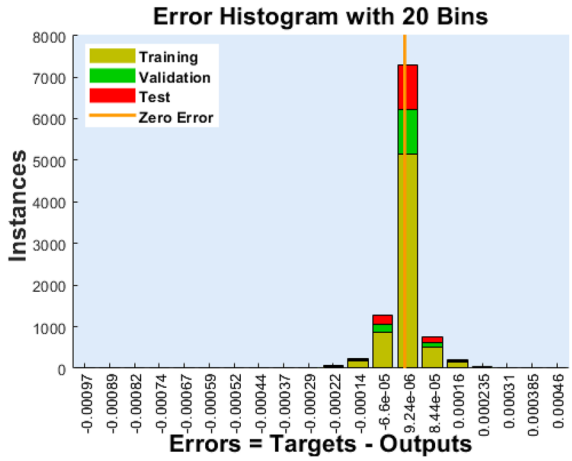

Case-1

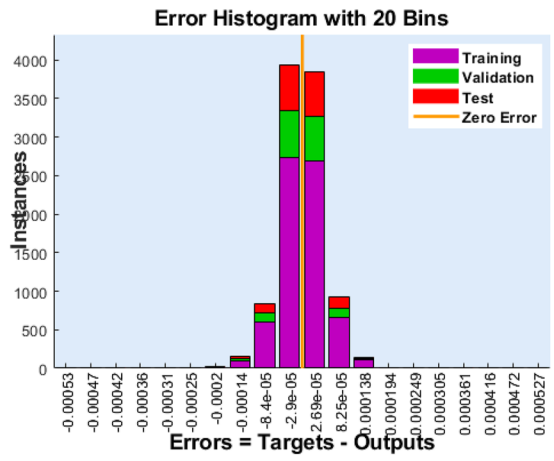

Case-2

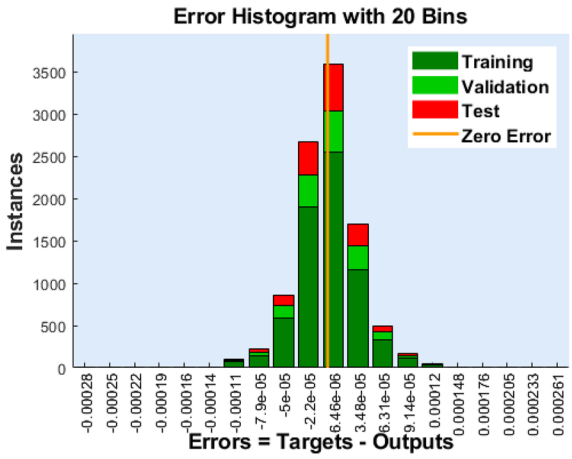

Case-3

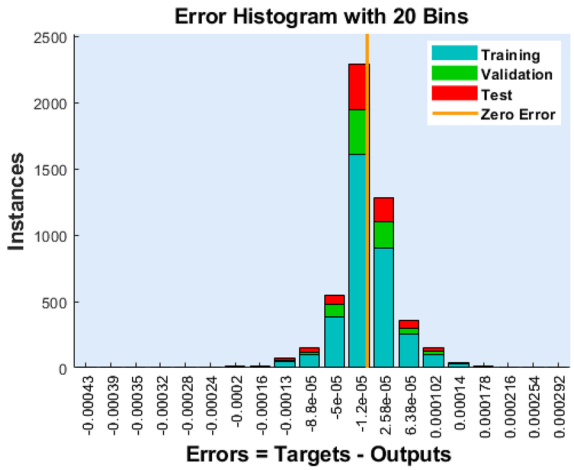

Case-4

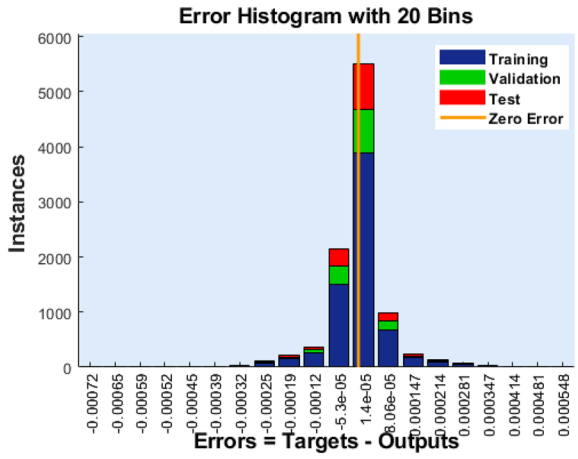

Case-5

FIG. 7. Error histogram (EH) values using the ANN-LMBOA to solve the EMHD-BCMN-TRS fluid model for case-1 to case-5.

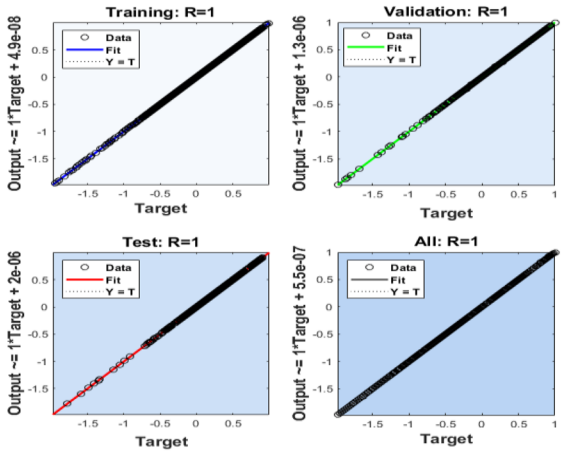

Case-1

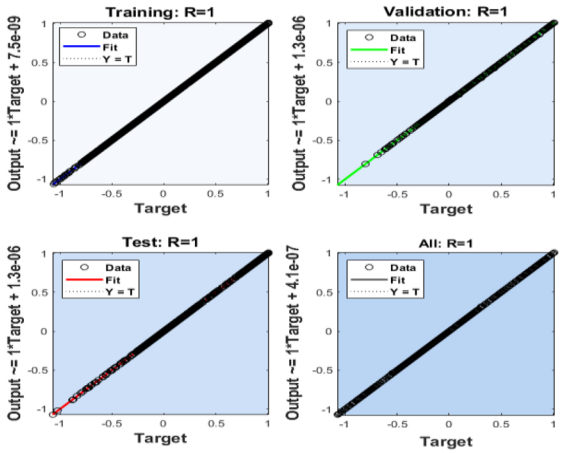

Case-2

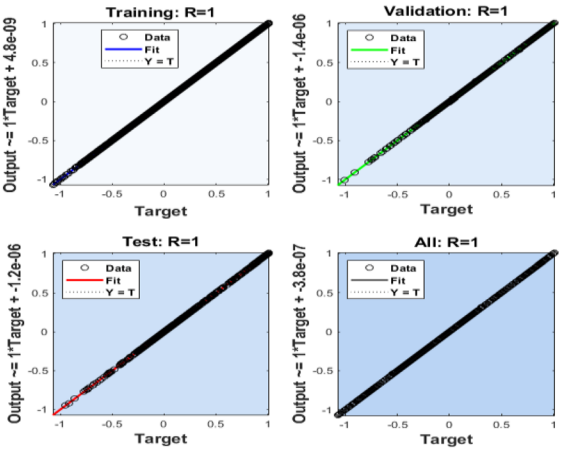

Case-3

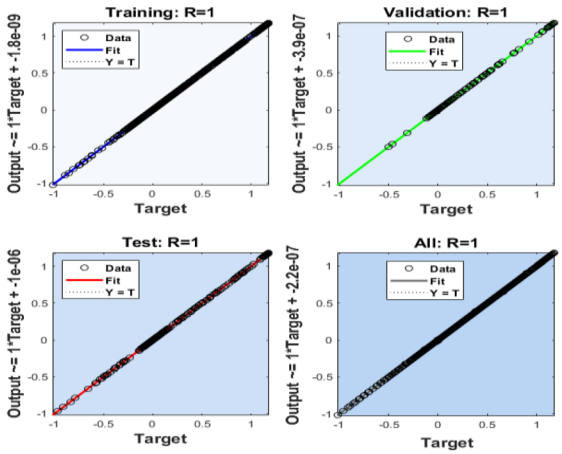

Case-4

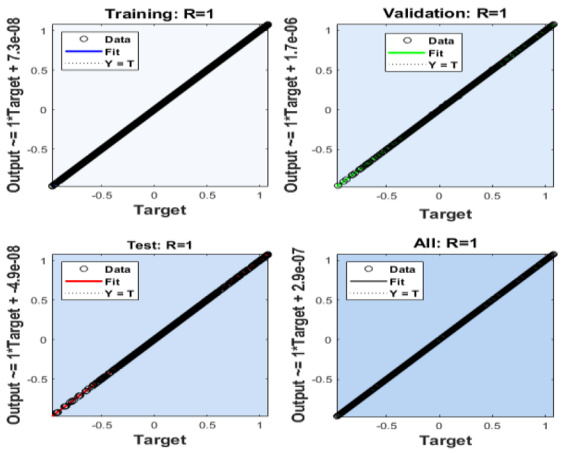

Case-5

FIG. 8. Regression measures through the ANN-LMBOA to solve the EMHD-BCMN-TRS fluid model for case-1 to case-5.

TABLE II. Results of ANN-LMBOA for EMHD-BCMN-TRS case 1.

	MSE							
Scenarios	Training	Validation	Testing	Performance	Gradient	Mu	Epoch	Time (s)
I	$3.085\,93 \times 10^{-9}$	$3.571\,91 \times 10^{-9}$	$3.964\,58 \times 10^{-9}$	3.09×10^{-9}	9.92×10^{-8}	1.00×10^{-8}	131	05
II	$2.765\,75 \times 10^{-9}$	$2.650\,51 \times 10^{-9}$	$2.709\,44 \times 10^{-9}$	2.77×10^{-9}	9.96×10^{-8}	1.00×10^{-8}	153	05
III	$3.276\,44 \times 10^{-9}$	$5.352\,22 \times 10^{-9}$	$3.466\,30 \times 10^{-9}$	3.28×10^{-9}	9.99×10^{-8}	1.00×10^{-8}	183	05
IV	$2.761\,99 \times 10^{-9}$	$3.911\,31 \times 10^{-9}$	$2.801\,47 \times 10^{-9}$	2.76×10^{-9}	9.87×10^{-8}	1.00×10^{-8}	149	06

TABLE III. Results of ANN-LMBOA for EMHD-BCMN-TRS case 2.

	MSE							
Scenarios	Train	Validation	Test	Performance	Gradient	Mu	Epoch	Time (s)
I	$2.470\,77 \times 10^{-9}$	$2.560\,14 \times 10^{-9}$	$3.209\,82 \times 10^{-9}$	2.47×10^{-9}	9.92×10^{-8}	1.00×10^{-8}	304	09
II	$2.187\,23 \times 10^{-9}$	$2.121\,33 \times 10^{-9}$	$2.474\,37 \times 10^{-9}$	2.19×10^{-9}	9.98×10^{-8}	1.00×10^{-8}	389	11
III	$2.612\,21 \times 10^{-9}$	$4.493\,07 \times 10^{-9}$	$2.564\,48 \times 10^{-9}$	2.61×10^{-9}	9.99×10^{-8}	1.00×10^{-8}	296	05
IV	$2.911\,78 \times 10^{-9}$	$2.476\,84 \times 10^{-9}$	$3.676\,61 \times 10^{-9}$	2.91×10^{-9}	9.95×10^{-8}	1.00×10^{-8}	340	10

TABLE IV. Results of ANN-LMBOA for EMHD-BCMN-TRS case 3.

	MSE							
Scenarios	Train	Validation	Test	Performance	Gradient	Mu	Epoch	Time (s)
I	$1.295\,41 \times 10^{-9}$	$1.312\,27 \times 10^{-9}$	$1.256\,84 \times 10^{-9}$	1.30×10^{-9}	9.97×10^{-8}	1.00×10^{-8}	530	16
II	$2.047\,04 \times 10^{-9}$	$2.021\,25 \times 10^{-9}$	$1.958\,23 \times 10^{-9}$	2.05×10^{-9}	1.00×10^{-7}	1.00×10^{-8}	430	12
III	$3.767\,58 \times 10^{-9}$	$3.431\,99 \times 10^{-9}$	$3.057\,10 \times 10^{-9}$	3.77×10^{-9}	9.89×10^{-8}	1.00×10^{-8}	186	05
IV	$3.713\,41 \times 10^{-9}$	$3.386\,98 \times 10^{-9}$	$3.759\,21 \times 10^{-9}$	3.71×10^{-9}	9.98×10^{-8}	1.00×10^{-8}	215	05

TABLE V. Results of ANN-LMBOA for EMHD-BCMN-TRS case 4.

	MSE							
Scenarios	Training	Validation	Testing	Performance	Gradient	Mu	Epoch	Time (s)
I	$2.076\,78 \times 10^{-9}$	$1.962\,46 \times 10^{-9}$	$2.643\,34 \times 10^{-9}$	2.08×10^{-9}	9.90×10^{-8}	1.00×10^{-9}	396	07
II	$2.179\,09 \times 10^{-9}$	$2.169\,62 \times 10^{-9}$	$1.963\,12 \times 10^{-9}$	2.18×10^{-9}	9.93×10^{-8}	1.00×10^{-9}	278	04
III	$1.891\,25 \times 10^{-9}$	$2.408\,92 \times 10^{-9}$	$1.722\,34 \times 10^{-9}$	1.89×10^{-9}	9.92×10^{-8}	1.00×10^{-9}	307	05
IV	$1.422\,54 \times 10^{-9}$	$1.877\,25 \times 10^{-9}$	$4.762\,96 \times 10^{-9}$	1.42×10^{-9}	9.99×10^{-8}	1.00×10^{-9}	274	05

TABLE VI. Results of ANN-LMBOA for EMHD-BCMN-TRS case 5.

	MSE							
Scenarios	Train	Validation	Test	Performance	Gradient	Mu	Epoch	Time (s)
I	$5.308\,07 \times 10^{-9}$	$9.131\,79 \times 10^{-9}$	$5.039\,22 \times 10^{-9}$	5.31×10^{-9}	9.94×10^{-8}	1.00×10^{-8}	120	03
II	$5.945\,80 \times 10^{-9}$	$6.542\,61 \times 10^{-9}$	$6.127\,59 \times 10^{-9}$	5.95×10^{-9}	9.87×10^{-8}	1.00×10^{-8}	129	06
III	$5.131\,41 \times 10^{-10}$	$5.302\,37 \times 10^{-10}$	$5.515\,82 \times 10^{-10}$	5.13×10^{-10}	9.93×10^{-8}	1.00×10^{-9}	271	08
IV	$3.131\,33 \times 10^{-10}$	$3.284\,25 \times 10^{-10}$	$3.390\,45 \times 10^{-10}$	3.13×10^{-10}	9.96×10^{-8}	1.00×10^{-9}	105	03

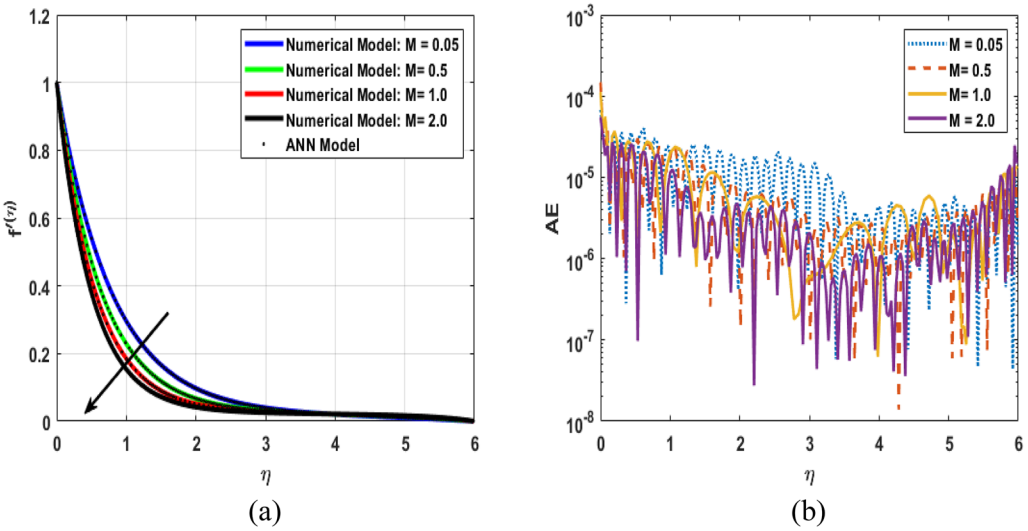

FIG. 9. Plots of the ANN-LMBO solution and errors for the velocity profile with the reference dataset of the EMHD-BCMN-TRS fluid model: (a) M *vs* $f'(\eta)$; (b) absolute error analysis.

be quantified using a variety of metrics, including accuracy, mean squared error, and robustness. The vector of a function's partial derivatives is referred to as the gradient in the context of neural networks. The gradient gives information about the orientation and strength of the loss function's sharpest ascent (or descent) in relation to the model parameters during training, which is numerically suggested in Tables II–VI. Utilizing methods of optimization such as gradient descent, the weights of the neural network are updated using these data. Without more context, "mu" might relate to the learning rate in various optimization methods, including gradient descent. Every time the neural network's weights are updated, the learning rate controls the step size. Selecting the right learning rate is essential for training convergence and stability. A hyperparameter called the learning rate determines how much the model is adjusted based on the anticipated error for each update of the model weights. Selecting the learning rate can be difficult since too small of a value could lead to an extended training process that could become stuck, while too large of a value could cause the training process to become

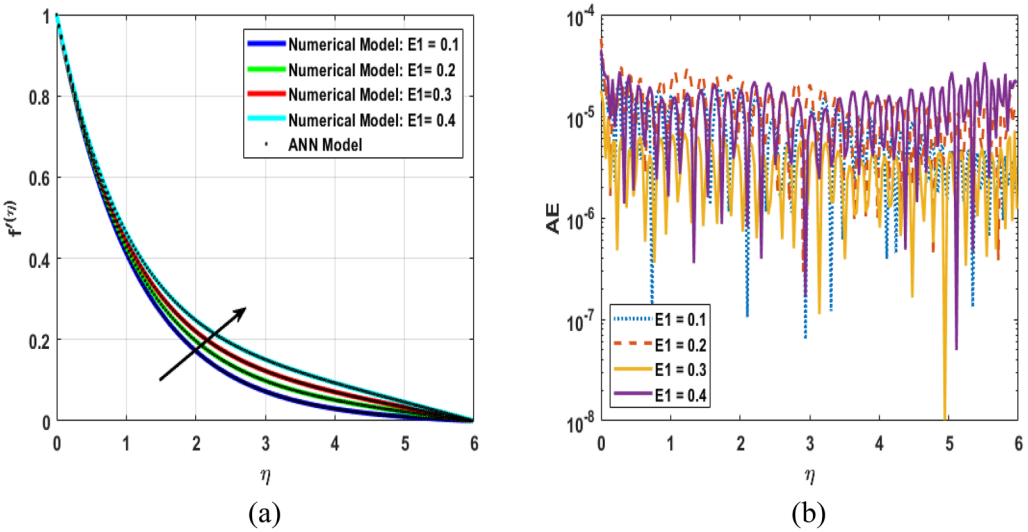

FIG. 10. Plots of the ANN-LMBO solution and errors for the velocity profile with the reference dataset of the EMHD-BCMN-TRS fluid model: (a) $E1$ *vs* $f'(\eta)$; (b) absolute error analysis.

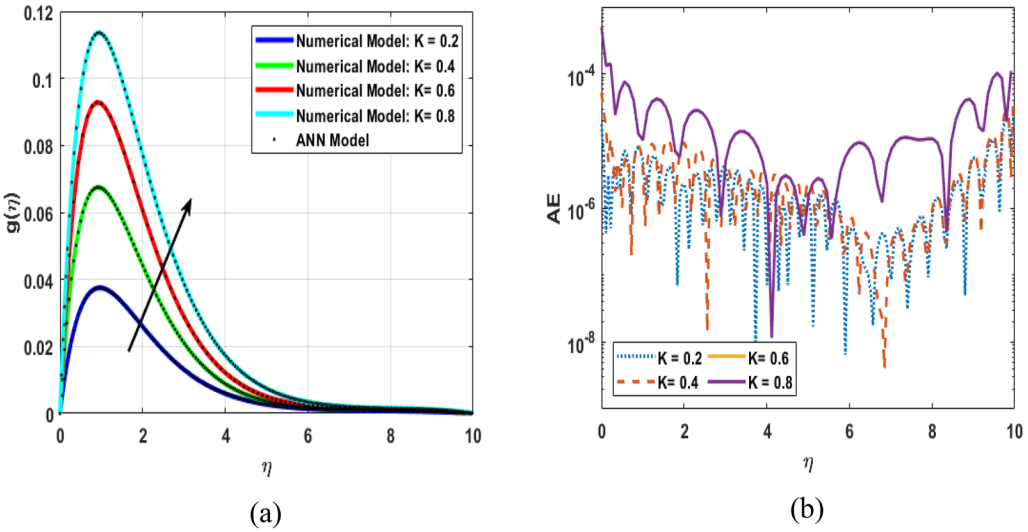

FIG. 11. Plots of the ANN-LMBO solution and errors for the angular velocity profile with the reference dataset of the EMHD-BCMN-TRS fluid model: (a) K *vs* $g(\eta)$; (b) absolute error analysis.

unstable or acquire a suboptimal set of weights too quickly. The numerical values of epoch listed in Tables II–VI describe a single forward and backward run of the neural network using all of the training instances. Put another way, the neural network sees the whole training dataset just once during a single epoch. Several epochs are usually used during training so that the model may iteratively learn from the data. The amount of time listed in Tables II–VI needed for inference, or generating predictions, on a dataset could be the time needed to train the neural network model. It offers information on the models and the training process's computing efficiency. The computational complexity of the algorithm is determined by measuring the amount of time needed to train networks, or to run all 1000 epochs, for the solution of the EMHD-BCMN-TRS fluid model. The results of the complexity analysis listed in Tables II–VI indicate that the ANN-LMBOA algorithm runs in around 10 ± 1 s for each of the four EMHD-BCMN-TRS fluid model instances. The comparison graphs and AE of the suggested and numerical solutions to solve the EMHD-BCMN-TRS fluid model are shown in Figs. 9(a)–18(b). It is shown that for every variation of the EMHD-BCMN-TRS fluid model, there was a perfect overlap between the

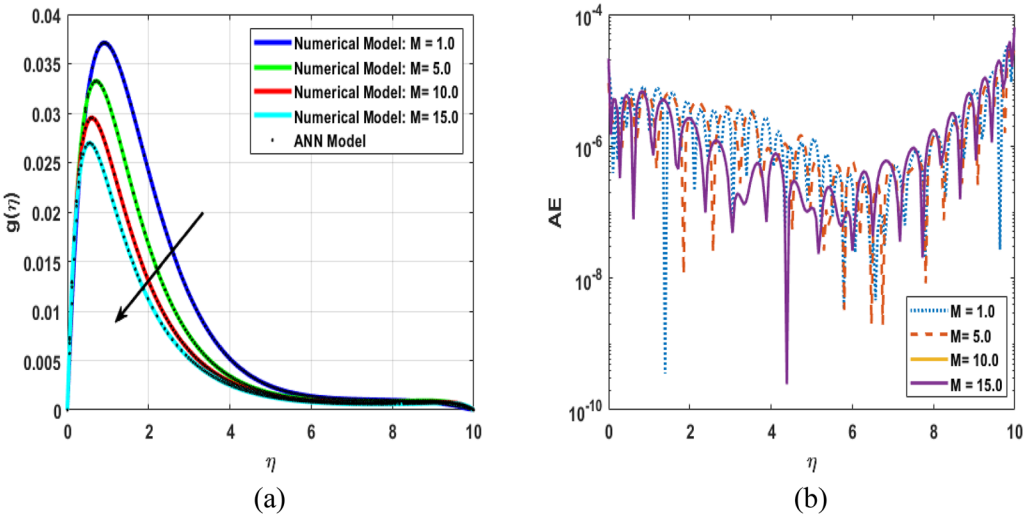

FIG. 12. Plots of the ANN-LMBO solution and errors for the angular velocity profile with the reference dataset of the EMHD-BCMN-TRS fluid model: (a) M *vs* $g(\eta)$; (b) absolute error analysis.

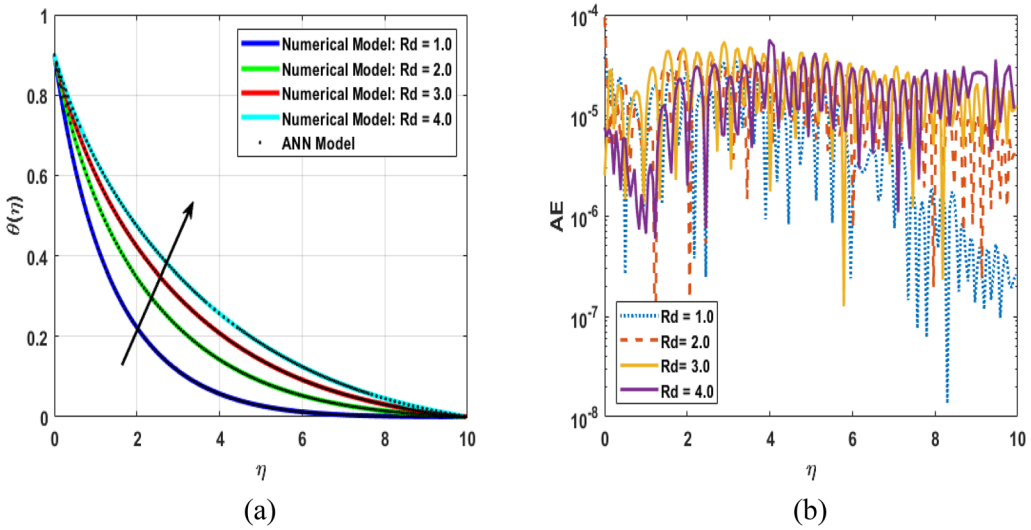

FIG. 13. Plots of the ANN-LMBO solution and errors for the temperature profile with the reference dataset of the EMHD-BCMN-TRS fluid model: (a) *Rd vs* $\theta(\eta)$; (b) absolute error analysis.

suggested and numerical results. The exactness and perfection of the designed ANN-LMBOA are indicated by the results' perfect overlap. The AE values for each case of the EMHD-BCMN-TRS fluid model are provided in Figs. 9(b)–18(b). Figures 9(b)–18(b) display the absolute error for each example determined from the reference numerical solutions, which, accordingly, demonstrates that the average AE is about 10^{-10}–10^{-3}. By employing the ANN-LMBOA, it is seen that the AE is found in good amounts for each case of the EMHD-BCMN-TRS fluid model. It is evident that the planned method for resolving the EMHD-BCMN-TRS fluid model is exact and accurate.

In order to examine the impact of different controlling factors emerging in the micropolar-type nanofluidic flow problem, the non-dimensional fluid profiles $\left(f'(\eta), g(\eta), \theta(\eta), \phi(\eta), \Psi(\eta)\right)$ are graphically illustrated in Figs 9(a)–18(a). These graphs illustrate the various values of non-dimensional parameters, i.e., magnetic number (M), electric field parameter $(E1)$, micropolar constant (K), thermal-radiation parameter (Rd), thermal stratification (S), mass

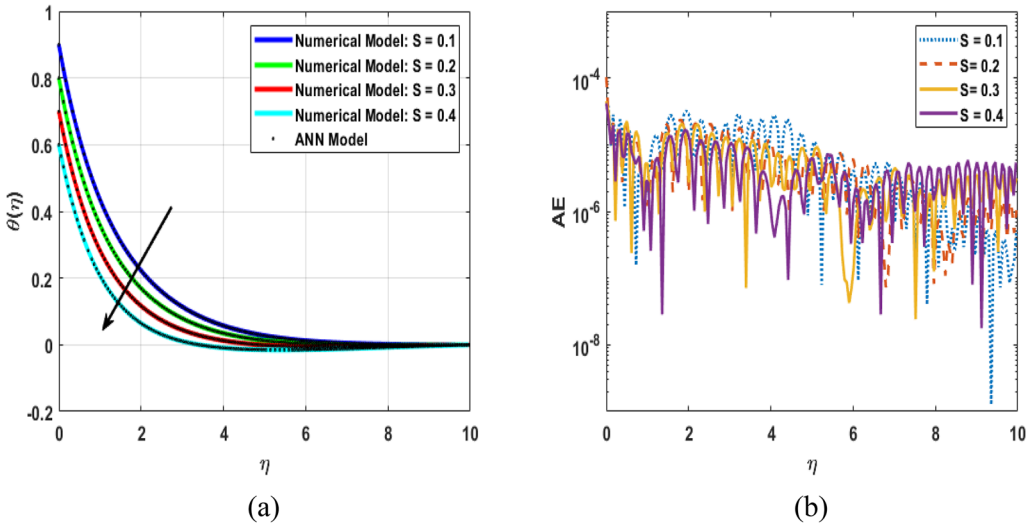

FIG. 14. Plots of the ANN-LMBO solution and errors for the temperature profile with the reference dataset of the EMHD-BCMN-TRS fluid model: (a) *S vs* $\theta(\eta)$; (b) absolute error analysis.

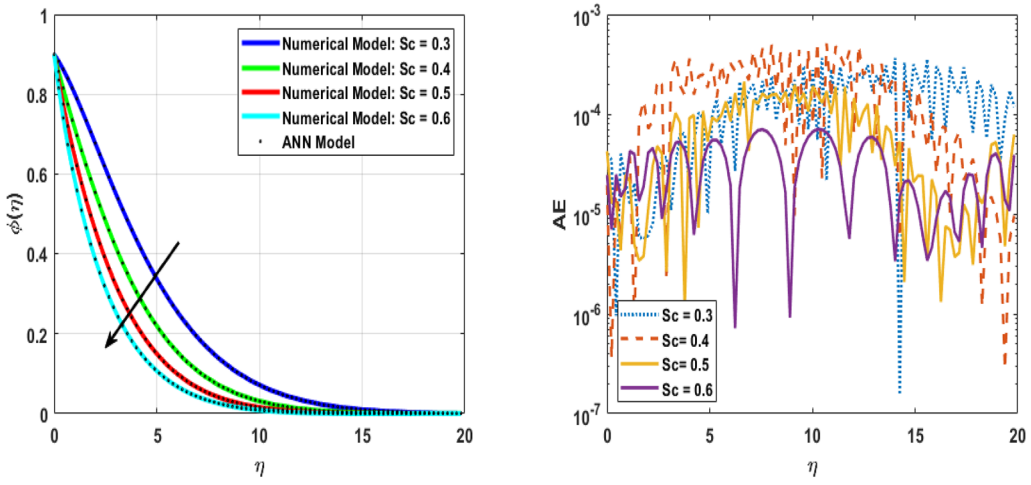

FIG. 15. Plots of the ANN-LMBO solution and errors for the concentration profile with the reference dataset of the EMHD-BCMN-TRS fluid model: (a) *Sc vs* $\phi(\eta)$; (b) absolute error analysis.

stratification parameters (Q), Schmidt number (Sc), and bioconvection Lewis parameter (Lb), on these $\left(f'(\eta), g(\eta), \theta(\eta), \phi(\eta), \Psi(\eta)\right)$ profiles. Figure 9(a) depicts the effect of a magnetic field parameter (M) on a velocity profile $\left(f'(\eta)\right)$. The thickness of the boundary layer and the $\left(f'(\eta)\right)$ profile are seen to both drop in response to a slight increase in the magnetic field, providing more evidence in favor of the magnetic field effect's regular convection. Due to the drag force produced by the magnetic effect, which causes the velocity field to decelerate, it can be demonstrated that as (M) increases, the velocity decreases. Figure 10(a) depicts the change in the velocity field profile $f'(\eta)$ caused by an electric field parameter $(E1)$. Enhancing the electric field parameter results in an increase in the velocity function. The electric field acts as a reducing force, reducing the fluid's frictional resistance and increasing the fluid's velocity. Figure 11(a) clarifies the relationship between the material parameter (K) and the angular field velocity $(g(\eta))$. The curvature of the impact in this graphical representation shows that $(g(\eta))$ is increased with increasing values of (K). Because of the increase in

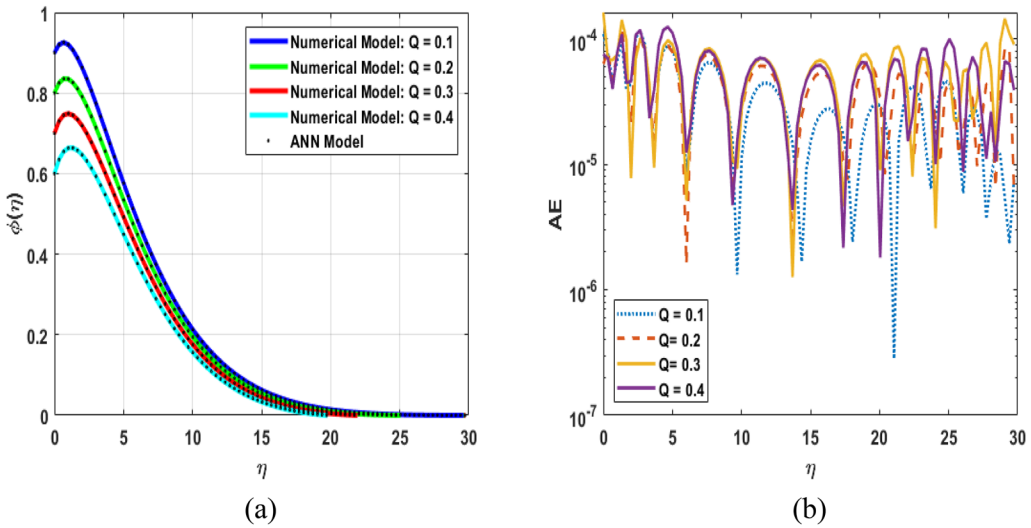

FIG. 16. Plots of the ANN-LMBO solution and errors for the concentration profile with the reference dataset of the EMHD-BCMN-TRS fluid model: (a) *Q vs* $\phi(\eta)$; (b) absolute error analysis.

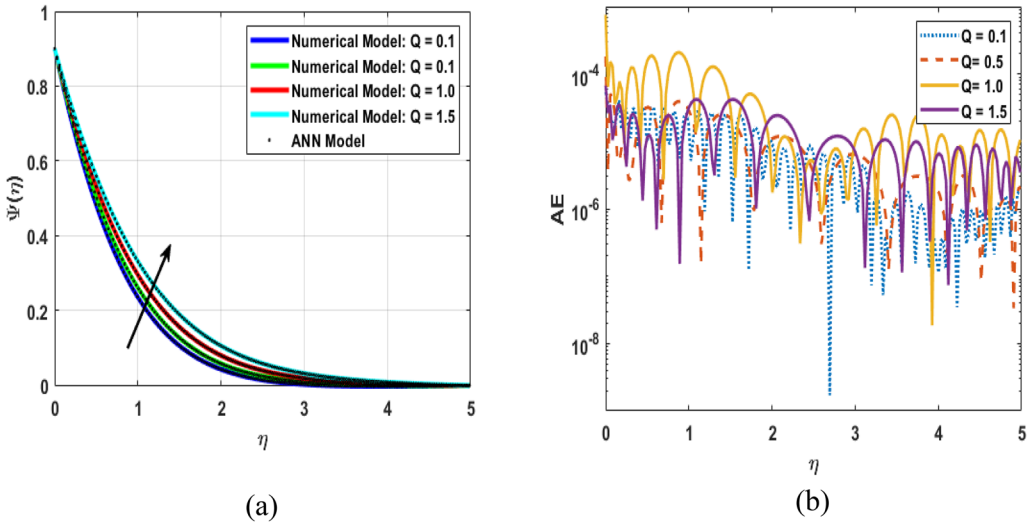

FIG. 17. Plots of the ANN-LMBO solution and errors for the micro-organism profile with the reference dataset of the EMHD-BCMN-TRS fluid model: (a) Q *vs* $\Psi(\eta)$; (b) absolute error analysis.

the nanofluid viscosity brought on by an acclivity in the material parameter, the angular flow speed has increased. The influence of the magnetic field number (M) on the angular velocity $(g(\eta))$ is investigated as shown in Fig. 12(a). By increasing the values of (M), the non-dimensional rotational field velocity $(g(\eta))$ decreases. An increase in (M) physically denotes an increase in the drag force, which is the opposing force that causes the angular velocity $(g(\eta))$ to decrease. By increasing the thermal radiation factor (Rd), as shown in Fig. 13(a), the temperature field $(\theta(\eta))$ is improved. The outcome shows that the corresponding boundary-layer formulation exhibits a significant shift in the energy profile even with a little change in thermal radiation bases. Figure 14(a) shows the effect of the thermal stratification parameter (S) on the energy field $(\theta(\eta))$. The nanofluid density in the inferior area is higher than that in the upper section due to increased heat stratification. As a result, the temperature difference between the ambient and heated exterior decreases, which results in a decrease in the nanofluid's energy field. Buoyancy forces and the thermal stratification parameter are strongly connected. When temperature gradients cause

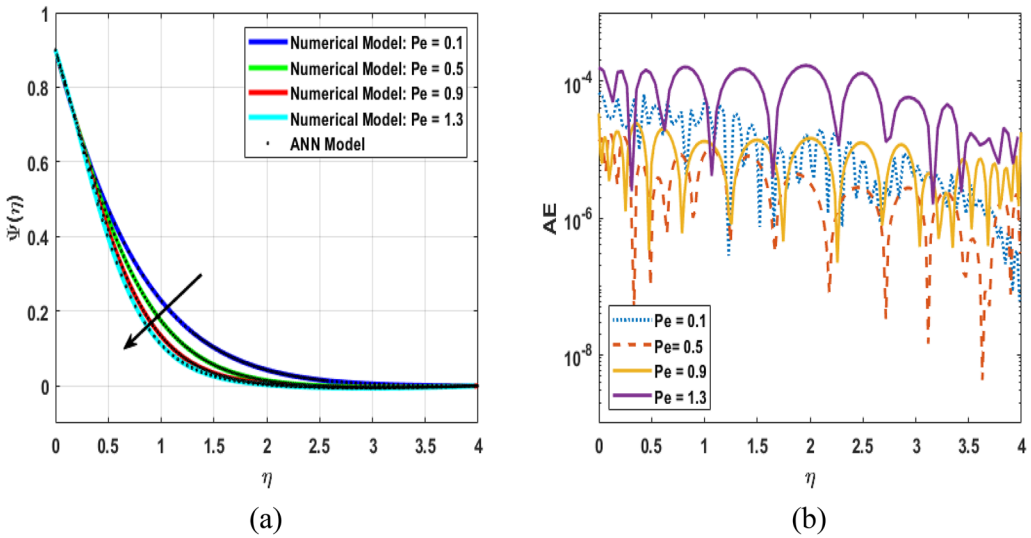

FIG. 18. Plots of the ANN-LMBO solution and errors for the micro-organism profile with the reference dataset of the EMHD-BCMN-TRS fluid model: (a) *Pe* *vs* $\Psi(\eta)$; (b) absolute error analysis.

fluid motion in natural convection scenarios, the thermal stratification parameter aids in measuring the impact of buoyancy on the flow. In addition, the thermal stratification parameter affects the thickness and properties of the thermal boundary layer in boundary layer flows, particularly those under the effect of temperature gradients. Figure 15(a) illustrates the concentration $\phi(\eta)$ behavior using different Schmidt number (Sc) values. The mass diffusivity to viscosity ratio is known as the Schmidt number. Due to the mass diffusion function being opposed to the Schmidt number, a decrease in mass-diffusion results from a decrease in nanoparticle density as the range of (Sc) is increased. Figure 16(a) shows the effect of the mass stratification parameter (Q). The behavior of the concentration boundary layer $\phi(\eta)$ and the associated BLT (boundary layer thickness) is reduced as parameter (Q) is increased. It is possible to define the variation in a substance's concentration close to barriers and interfaces by including the mass stratification parameter under boundary conditions. To effectively capture the impact of species mobility, the mass stratification parameter can be used to indicate the choice of boundary conditions for concentration gradients. The behavior of the microbial density $(\Psi(\eta))$ field is increased by the progressively and slowly increasing range of the mass stratification (Q) factor, as shown in Fig. 17(a). The microbe's density $(\Psi(\eta))$ profile is highlighted in Fig. 18(a) for various values of the bioconvection Lewis (Lb) number. A higher magnitude of the number denotes a reduction in microbial diffusion, which is evident in the density profile.

VIII. CONCLUSION

An innovative solution to this challenging issue is to apply the Levenberg–Marquardt (LM) technique and computational numerical scheme for EMHD bioconvection flow of micropolar nanofluid with an induced thermal radiation and stratification effect. Approximating the solutions to a collection of nonlinear equations is made possible by the LM approach, which is acknowledged as a powerful optimization tool. Our computational architecture's fundamental approach, the numerical method, is a reliable way to solve higher order differential equations. In EMHD bioconvection flow of the micropolar nanofluid flow regime, we use the LM approach to solve the governing equations of fluid flow and then apply it to find the best values of key parameters. These metrics include profiles such as temperature, concentration, and fluid velocity. The ramifications of our findings go beyond mere theoretical progress. Our neural network method and computational framework yield insights that may be used to real-world fluid system optimization. Future work can consider including additional physical components and more intricate fluid dynamics by broadening the scope of our computational approach. We can improve the accuracy and efficiency of our surrogate models by implementing new neural network topologies and training techniques. Our work paves the path for future innovation and advancement in fluid dynamics research and applications by offering a solid foundation for future study and development of computational approaches in EMHD bioconvection flow of micropolar nanofluid flow. The best compatibility is achieved at about 10^{-2}–10^{-8}, which means that the consistent accuracy of the ANN-LMBAO algorithm is successfully simulated. Furthermore, following are a few noteworthy findings that briefly demonstrate the effects of leading parameters:

- To show the dynamics of the underlying mathematical form of the system model, the governing relations are shown in a differential system.
- Reference datasets for the proposed model were produced under various scenarios by the bvp4c numerical solver. These datasets were effectively employed as inputs and targets of LMLA-BPNN to predict approximate solutions for each scenario.
- Several situations with magnetic, electric, and vertex viscosity, thermal radiation, chemical reaction, Schmidt number, mass stratification, and Peclet number have been simulated utilizing the ANN-LMBAO method and computing system. This feature makes it a helpful tool for researching the EMHD-BCMN-TRS fluid model over a stretchable plate.
- An effective optimization technique for approximating the solution of a system of nonlinear equations is the LMLA-BPNN approach. Consequently, it can be effectively utilized to resolve the difficult equations that describe the EMHD-BCMN-TRS fluid model across a stretchable plate.
- The results of performance evaluation, including the regression index and error histogram analysis, are combined for every EMHD-BCMN-TRS fluid model scenario.
- The applicability of ANN-LMBAO for solving models of nanofluids with the accuracy in the range 10×10^{-8}–10×10^{-3} is often demonstrated through comparison studies. This is determined by subtracting the absolute difference between the reference results and the mean square error of the convergence curves.
- The velocity profile increases when the electrical field coefficient is high and decreases when the magnetic field is strong.
- The magnetic parameter causes an increase in angular velocity, whereas the material parameter causes a decrease.
- Thermal stratification and electric field parameters cause the energy profile to decrease, but thermal radiation variation causes it to increase.
- Because of the increasing effects of mass stratification, the strength of nanofluid concentration increases.
- As Lewis number and Peclet number ranges increase and as the material parameter increases, the density of microbe concentration weakens.

ACKNOWLEDGMENTS

The authors acknowledge Princess Nourah bint Abdulrahman University Researchers Supporting Project No. PNURSP2024R 371, Princess Nourah bint Abdulrahman University, Riyadh, Saudi Arabia.

Nisreen Innab would like to express her sincere gratitude to AlMaarefa University, Riyadh, Saudi Arabia, for providing funding to conduct this research.

AUTHOR DECLARATIONS

Conflict of Interest

The authors have no conflicts to disclose.

Author Contributions

Zeeshan Khan: Conceptualization (equal); Data curation (equal); Methodology (equal); Writing – original draft (equal). **Wafa F. Alfwzan**: Formal analysis (equal); Investigation (equal); Software (equal); Validation (equal). **Aatif Ali**: Investigation (equal); Methodology (equal); Software (equal). **Nisreen Innab**: Data curation (equal); Methodology (equal); Writing – review & editing (equal). **Samina Zuhra**: Investigation (equal); Resources (equal); Writing – original draft (equal); Writing – review & editing (equal). **Saeed Islam**: Formal analysis (equal); Supervision (equal); Visualization (equal). **Joshua Kiddy K. Asamoah**: Formal analysis (equal); Resources (equal); Visualization (equal); Writing – review & editing (equal).

DATA AVAILABILITY

The data that support the findings of this study are available within the article and also provided on reasonable request.

REFERENCES

[1] S. U. S. Choi, Nanofluid technology: Current status and future research (No. ANL/ET/CP-97466), Argonne National Lab (ANL), Argonne, IL (USA), 1998.

[2] I. Manna, "Synthesis, characterization and application of nanofluid—An overview," J. Indian Inst. Sci. **89**(1), 21–33 (2009).

[3] L. Zhang, T. Nazar, M. M. Bhatti, and E. E. Michaelides, "Stability analysis on the kerosene nanofluid flow with hybrid zinc/aluminum-oxide (ZnO-Al_2O_3) nanoparticles under Lorentz force," Int. J. Numer. Methods Heat Fluid Flow **32**, 740 (2021).

[4] Y. Geng, A. A. Al-Rashed, B. Mahmoudi, A. S. Alsagri, A. Shahsavar, and P. Talebizadehsardari, "Characterization of the nanoparticles, the stability analysis and the evaluation of a new hybrid nano-oil thermal conductivity," J. Therm. Anal. Calorim. **139**(2), 1553–1564 (2020).

[5] R. Choudhary, D. Khurana, A. Kumar, and S. Subudhi, "Stability analysis of Al_2O_3/water nanofluids," J. Exp. Nanosci. **12**(1), 140–151 (2017).

[6] L. Fedele, L. Colla, S. Bobbo, S. Barison, and F. Agresti, "Experimental stability analysis of different water-based nanofluids," Nanoscale Res. Lett. **6**(1), 300–308 (2011).

[7] T. Hayat, M. Rashid, M. Imtiaz, and A. Alsaedi, "Magnetohydrodynamic (MHD) stretched flow of nanofluid with power-law velocity and chemical reaction," AIP Adv. **5**(11), 117121 (2015).

[8] N. S. Khashi'ie, N. M. Arifin, and I. Pop, "Magnetohydrodynamics (MHD) boundary layer flow of hybrid nanofluid over a moving plate with Joule heating," Alexandria Eng. J. **61**(3), 1938–1945 (2022).

[9] Y. M. Chu, S. Bashir, M. Ramzan, and M. Y. Malik, "Model-based comparative study of magnetohydrodynamics unsteady hybrid nanofluid flow between two infinite parallel plates with particle shape effects," Math. Methods Appl. Sci. **46**, 11568 (2022).

[10] A. Khentout, M. Kezzar, M. R. Sari, T. Ismail, M. S. Tich Tich, S. Boutelba, and M. R. Eid, "The electrical magnetohydrodynamic (MHD) and shape factor impacts in a mixture fluid suspended by hybrid nanoparticles between non-parallel plates," Proc. Inst. Mech. Eng., Part E **236**(3), 1134–1143 (2022).

[11] A. M. Alqahtani, M. Bilal, A. Ali, H. A. E. W. Khalifa, and H. Alqahtani, "Numerical calculation of unsteady MHD nanofluid flow across two fluctuating discs with chemical reaction and zero mass flux," Z. Angew. Math. Mech. e20230001 (published online, 2023).

[12] A. Dawar, A. Wakif, T. Thumma, and N. A. Shah, "Towards a new MHD non-homogeneous convective nanofluid flow model for simulating a rotating inclined thin layer of sodium alginate-based iron oxide exposed to incident solar energy," Int. Commun. Heat Mass Transfer **130**, 105800 (2022).

[13] K. A. M. Alharbi, M. Bilal, A. Ali, S. M. Eldin, A. F. Soliman, and M. U. Rahman, "Stagnation point flow of hybrid nanofluid flow passing over a rotating sphere subjected to thermophoretic diffusion and thermal radiation," Sci. Rep. **13**(1), 19093 (2023).

[14] A. C. Eringen, "Simple microfluids," Int. J. Eng. Sci. **2**(2), 205–217 (1964).

[15] A. C. Eringen, "Theory of micropolar fluids," Indiana Univ. Math. J. **16**, 1–18 (1966).

[16] A. C. Eringen, "Theory of thermomicrofluids," J. Math. Anal. Appl. **38**(2), 480–496 (1972).

[17] P. K. Pattnaik, M. M. Bhatti, S. R. Mishra, M. A. Abbas, and O. A. Bég, "Mixed convective-radiative dissipative magnetized micropolar nanofluid flow over a stretching surface in porous media with double stratification and chemical reaction effects: ADM-Padé computation," J. Math. **2022**, 9888379.

[18] M. Bilal, A. Saeed, T. Gul, W. Kumam, S. Mukhtar, and P. Kumam, "Parametric simulation of micropolar fluid with thermal radiation across a porous stretching surface," Sci. Rep. **12**(1), 2542 (2022).

[19] F. Mabood, M. D. Shamshuddin, and S. R. Mishra, "Characteristics of thermophoresis and Brownian motion on radiative reactive micropolar fluid flow towards continuously moving flat plate: HAM solution," Math. Comput. Simul. **191**, 187–202 (2022).

[20] P. Pasha, S. Mirzaei, and M. Zarinfar, "Application of numerical methods in micropolar fluid flow and heat transfer in permeable plates," Alexandria Eng. J. **61**(4), 2663–2672 (2022).

[21] S. R. R. Reddy and P. B. Anki Reddy, "Numerical simulations of unsteady 3D MHD micropolar fluid flow over a slendering sheet," J. Appl. Comput. Mech. **7**(3), 1403 (2020).

[22] N. A. Hill and T. J. Pedley, "Bioconvection," Fluid Dyn. Res. **37**(1–2), 1 (2005).

[23] S. U. Khan, S. A. Shehzad, and N. Ali, "Bioconvection flow of magnetized Williamson nanoliquid with motile organisms and variable thermal conductivity," Appl. Nanosci. **10**(8), 3325–3336 (2020).

[24] S. Abdal, I. Siddique, D. Alrowaili, Q. Al-Mdallal, and S. Hussain, "Exploring the magnetohydrodynamic stretched flow of Williamson Maxwell nanofluid through porous matrix over a permeated sheet with bioconvection and activation energy," Sci. Rep. **12**(1), 278 (2022).

[25] D. Habib, N. Salamat, S. Abdal, I. Siddique, M. C. Ang, and A. Ahmadian, "On the role of bioconvection and activation energy for time dependent nanofluid slip transpiration due to extending domain in the presence of electric and magnetic fields," Ain Shams Eng. J. **13**(1), 101519 (2022).

[26] B. Ali, A. Shafiq, A. Manan, A. Wakif, and S. Hussain, "Bioconvection: Significance of mixed convection and MHD on dynamics of Casson nanofluid in the stagnation point of rotating sphere via finite element simulation," Math. Comput. Simul. **194**, 254–268 (2022).

[27] E. A. Algehyne, M. Areshi, A. Saeed, M. Bilal, W. Kumam, and P. Kumam, "Numerical simulation of bioconvective Darcy–Forchhemier nanofluid flow with energy transition over a permeable vertical plate," Sci. Rep. **12**(1), 3228 (2022).

[28] S. Zuhra, N. S. Khan, Z. Shah, S. Islam, and E. Bonyah, "Simulation of bioconvection in the suspension of second grade nanofluid containing nanoparticles and gyrotactic microorganisms," AIP Adv. **8**(10), 105210 (2018).

[29] S. Zuhra, N. S. Khan, and S. Islam, "Magnetohydrodynamic second-grade nanofluid flow containing nanoparticles and gyrotactic microorganisms," Comput. Appl. Math. **37**(5), 6332–6358 (2018).

[30] M. J. Khan, S. Zuhra, R. Nawaz, B. Duraisamy, M. S. Alqahtani, K. S. Nisar, and W. Jamshed, and M. Abbas, "Numerical analysis of bioconvection-MHD flow of Williamson nanofluid with gyrotactic microbes and thermal radiation: New iterative method," Open Phys. **20**(1), 470–483 (2022).

[31] A. Saeed and T. Gul, "Bioconvection Casson nanofluid flow together with Darcy–Forchheimer due to a rotating disk with thermal radiation and arrhenius activation energy," SN Appl. Sci. **3**(1), 78 (2021).

[32] A. Shahzad, M. Imran, M. Tahir, S. Ali Khan, A. Akgül, S. Abdullaev, C. Park, H. Y. Zahran, and I. S. Yahia, "Brownian motion and thermophoretic diffusion impact on Darcy–Forchheimer flow of bioconvective micropolar nanofluid between double disks with Cattaneo–Christov heat flux," Alexandria Eng. J. **62**, 1 (2023).

[33] D. Habib, N. Salamat, M. Ahsan, S. Abdal, I. Siddique, and B. Ali, "Significance of bioconvection and mass transpiration for MHD micropolar Maxwell nanofluid flow over an extending sheet," Waves Random Complex Media (published online, 2022).

[34] L. Ali, X. Liu, B. Ali, S. Mujeed, and S. Abdal, "Finite element simulation of multi-slip effects on unsteady MHD bioconvective micropolar nanofluid flow over

a sheet with solutal and thermal convective boundary conditions," Coatings **9**(12), 842 (2019).
[35]I. Tlili, M. Ramzan, H. Un Nisa, M. Shutaywi, Z. Shah, and P. Kumam, "Onset of gyrotactic microorganisms in MHD micropolar nanofluid flow with partial slip and double stratification," J. King Saud Univ. Sci. **32**(6), 2741–2751 (2020).
[36]A. Agrawal and A. Choudhary, "Perspective: Materials informatics and big data: Realization of the 'fourth paradigm' of science in materials science," APL Mater. **4**(5), 053208 (2016).
[37]M. Frank, D. Drikakis, and V. Charissis, "Machine-learning methods for computational science and engineering," Computation **8**(1), 15 (2020).
[38]T. Wang, C. Zhang, H. Snoussi, and G. Zhang, "Machine learning approaches for thermoelectric materials research," Adv. Funct. Mater. **30**(5), 1906041 (2020).
[39]S. L. Brunton, M. S. Hemati, and K. Taira, "Special issue on machine learning and data-driven methods in fluid dynamics," Theor. Comput. Fluid Dyn. **34**(4), 333–337 (2020).
[40]F. Sofos, C. Stavrogiannis, K. K. Exarchou-Kouveli, D. Akabua, G. Charilas, and T. E. Karakasidis, "Current trends in fluid research in the era of artificial intelligence: A review," Fluids **7**(3), 116 (2022).
[41]O. E. Agwu, J. U. Akpabio, S. B. Alabi, and A. Dosunmu, "Artificial intelligence techniques and their applications in drilling fluid engineering: A review," J. Pet. Sci. Eng. **167**, 300–315 (2018).
[42]W. W. Zhang and B. R. Noack, "Artificial intelligence in fluid mechanics," Acta Mech. Sin. **37**(12), 1715–1717 (2021).
[43]S. Jakeer, M. Lakshmi Rupa, S. R. Reddisekhar Reddy, and A. M. Rashad, "Artificial neural network model of non-Darcy MHD Sutterby hybrid nanofluid flow over a curved permeable surface: Solar energy applications," Propuls. Power Res. **12**(3), 410–427 (2023).
[44]S. R. R. Reddy, S. Jakeer, and M. L. Rupa, "ANN model of three-dimensional micropolar dusty hybrid nanofluid flow with coriolis force: Biomedical applications," Indian J. Phys. **97**, 3801–3825 (2023).
[45]A. V. Anand, R. Ali, S. Jakeer, and S. R. R. Reddy, "Entropy-optimized MHD three-dimensional solar slendering sheet of micropolar hybrid nanofluid flow using a machine learning approach," J. Therm. Anal. Calorim. (published online, 2023).
[46]M. A. Z. Raja, Z. Khan, S. Zuhra, N. I. Chaudhary, W. U. Khan, Y. He, S. Islam, and M. Shoaib, "Cattaneo–Christov heat flux model of 3D hall current involving biconvection nanofluidic flow with Darcy–Forchheimer law effect: Backpropagation neural networks approach," Case Stud. Therm. Eng. **26**, 101168 (2021).
[47]A. Shafiq, A. B. Çolak, and T. N. Sindhu, "Development of an intelligent computing system using neural networks for modeling bioconvection flow of second-grade nanofluid with gyrotactic microorganisms," Numer. Heat Transfer, Part B (published online, 2023).
[48]A. Shafiq, A. B. Çolak, and T. N. Sindhu, "Significance of EMHD graphene oxide (GO) water ethylene glycol nanofluid flow in a Darcy–Forchheimer medium by machine learning algorithm," Eur. Phys. J. Plus **138**(3), 213 (2023).
[49]S. M. Atif, S. Hussain, and M. Sagheer, "Magnetohydrodynamic stratified bio-convective flow of micropolar nanofluid due to gyrotactic microorganisms," AIP Adv. **9**(2), 025208 (2019).
[50]K. L. Hsiao, "Micropolar nanofluid flow with MHD and viscous dissipation effects towards a stretching sheet with multimedia feature," Int. J. Heat Mass Transfer **112**, 983–990 (2017).
[51]Z. Khan, S. Zuhra, S. Islam, M. A. Z. Raja, and A. Ali, "Modeling and simulation of Maxwell nanofluid flows in the presence of Lorentz and Darcy–Forchheimer forces: Toward a new approach on Buongiorno's model using artificial neural network (ANN)," Eur. Phys. J. Plus **138**(1), 107 (2023).
[52]A. Ali, N. A. Ahammad, E. Tag-Eldin, F. Gamaoun, Y. I. Daradkeh, and M. F. Yassen, "MHD Williamson nanofluid flow in the rheology of thermal radiation, Joule heating, and chemical reaction using the Levenberg–Marquardt neural network algorithm," Front. Energy Res. **10**, 1175 (2022).
[53]M. Y. Shams, O. M. Elzeki, L. M. Abouelmagd, A. E. Hassanien, M. A. Elfattah, and H. Salem, "HANA: A healthy artificial nutrition analysis model during COVID-19 pandemic," Comput. Biol. Med. **135**, 104606 (2021).
[54]M. A. Z. Raja, M. Shoaib, Z. Khan, S. Zuhra, C. A. Saleel, K. S. Nisar, S. Islam, and I. Khan, "Supervised neural networks learning algorithm for three dimensional hybrid nanofluid flow with radiative heat and mass fluxes," Ain Shams Eng. J. **13**(2), 101573 (2022).
[55]S. Nasir, A. S. Berrouk, T. Gul, and A. Ali, "Develop the artificial neural network approach to predict thermal transport analysis of nanofluid inside a porous enclosure," Sci. Rep. **13**(1), 21039 (2023).
[56]O. M. Elzeki, M. Abd Elfattah, H. Salem, A. E. Hassanien, and M. Shams, "A novel perceptual two layer image fusion using deep learning for imbalanced COVID-19 dataset," PeerJ Comput. Sci. **7**, e364 (2021).